Micro- and nanostructural investigations of high and ultra-high performance concrete under fatigue

Michael Engelhardt, Andreas Kalytta-Mewes, Dirk Volkmer, Jessica Lohmann, Martin Ritter, Gunnar Schaan, Frank Schmidt-Döhl, Mohamed Abubakar Ali, Marco Basaldella, Michael Haist, Bianca Kern, Ludger Lohaus, Nadja Oneschkow, Corinna Rozanski, Tim Timmermann, Christian U. Grosse, Veit Birtel, Harald Garrecht, Hamid Madadi, Martin Markert, Holger Steeb

Angaben zur Veröffentlichung / Publication details:

Engelhardt, Michael, Andreas Kalytta-Mewes, Dirk Volkmer, Jessica Lohmann, Martin Ritter, Gunnar Schaan, Frank Schmidt-Döhl, et al. 2025. “Micro- and nanostructural investigations of high and ultra-high performance concrete under fatigue.” International Journal of Fatigue 199: 109038. https://doi.org/10.1016/j.ijfatigue.2025.109038.

International Journal of Fatigue 199 (2025) 109038

Contents lists available at ScienceDirect

International Journal of Fatigue

journal homepage: www.elsevier.com/locate/ijfatigue

Micro- and nanostructural investigations of high and ultra-high performance concrete under fatigue

Michael Engelhardt [a], Andreas Kalytta-Mewes [a], Dirk Volkmer [a], Jessica Lohmann [b], Martin Ritter [b], Gunnar Schaan [b], Frank Schmidt-Döhl [b,*], Mohamed Abubakar Ali [c], Marco Basaldella [c], Michael Haist [c], Bianca Kern [c], Ludger Lohaus [c], Nadja Oneschkow [c], Corinna Rozanski [c], Tim Timmermann [c], Christian U. Grosse [d], Veit Birtel [e], Harald Garrecht [e], Hamid Madadi [e], Martin Markert [e], Holger Steeb [e]

[a] *University of Augsburg, Universitätsstraße 2, 86159 Augsburg, Germany*
[b] *Hamburg University of Technology, Am Schwarzenberg-Campus 1, 21073 Hamburg, Germany*
[c] *Leibniz University Hannover, Welfengarten 1, 30167 Hannover, Germany*
[d] *Technical University of Munich, Arcisstraße 21, 80333 Munich, Germany*
[e] *University of Stuttgart, Keplerstraße 7, 70174 Stuttgart, Germany*

ARTICLE INFO

Keywords:
Fatigue
HPC
UHPC
Microstructure
Testing Methods

ABSTRACT

A fine-grained UHPC, both undamaged and damaged by fatigue loading, was comparatively examined by various microstructural analytical methods, to evaluate the different techniques with respect to their applicability and relevance for the investigation of fatigue damage processes. The fatigue tests were stopped at the transition from phase II to phase III of the s-shaped strain development. The cyclic compression loading was performed with a frequency of $f_t = 1$ Hz, and a stress level between $S_{min} = 0.05$ and $S_{max} = 0.75$ ($f_{cm} = 170.2$ MPa). The fatigue process under these loading conditions is dominated by alterations and damages on the nano-scale, that can be observed by transmission electron microscopy. The resulting coarsening of the pore structure was also visible with dynamic vapor sorption. Nanoindentation indicates, that changes of the HD-C-S-H-phase occur. IR spectroscopy also indicates changes of the C-S-H phase and thermal analysis changes of the water content. Dynamic mechanical analysis (DMA) gave insight into the complex Young's modulus and Poisson's ratio changes. The acoustic emission technique gives information on the different processes during the single phases of fatigue and reveal a very different damage behaviour of dry and moist materials. Some microcracks are visible with light microscopy. It appears, that the number of cracks after fatigue is higher than before. With X-ray computed tomography, X-ray powder diffraction, the drying behaviour, the free water uptake, the water uptake under vacuum and by mercury intrusion porosimetry no significant differences between specimens with and without fatigue loading could be observed in this examination.

1. Introduction

The usage of concretes with ever-higher strengths allows for the construction of more filigree and slender structures with reduced self-weight. Furthermore, resource-saving structures are also characterised by a higher slenderness. For these structures, the fatigue resistance is relevant, and even more so for structures inevitably subjected to cyclic loads, e.g. bridges or wind energy turbines. However, despite the long history of concrete fatigue research very little knowledge is available concerning the damage processes in the concretés microstructure when exposed to fatigue loading. This lack of knowledge is one of the main reasons why the design regulations in currently valid standards or guidelines (e.g. [1,2]) are very conservative, especially for high-strength and ultra-high strength concretes.

Therefore, the overall aim of the priority programme (SPP) 2020 "Cyclic Deterioration of High-Performance Concrete in an Experimental-Virtual-Lab" funded by the German Research Foundation was to understand, describe, model and predict the material degradation of high-

* Corresponding author.
E-mail address: schmidt-doehl@tuhh.de (F. Schmidt-Döhl).

https://doi.org/10.1016/j.ijfatigue.2025.109038
Received 4 February 2025; Received in revised form 2 April 2025; Accepted 29 April 2025
Available online 30 April 2025

performance concretes due to fatigue loading. The fatigue behaviour of high-performance concretes is investigated within differently focused projects [3]. It already became clear that the damage propagation in the concrete microstructure due to compressive fatigue loading starts and develops on a very small scale. This is concurrently one of the main challenges in research: For the observation and investigation of these damage processes, the investigation techniques available must be combined and used at the limits of their applicability in order to gain new knowledge. Thus, coordinated research was conducted within the SPP 2020 for the purpose of comparison and evaluation of different techniques of microstructural analyses with respect to their applicability and relevance for the investigation of the damage processes in the concrete's microstructure. This paper summarises the main results of this conjoint research activity.

2. Examined Ultra-High strength concrete (UHPC)

The investigations were conducted on the reference ultra-high strength concrete used in the priority programme 2020 (named "RU1") [4,5]. It was developed based on the fine-grained mixture M3Q previously used in the priority programme 1182 [6] and has no steel fibers inside. The composition of the RU1 concrete is given in Table 1.

The cement used is a rapidly hardening Portland cement with high sulfate resistance and low effective alkali content. Its chemical composition can be found in Table 2.

Silica fume completes the binder in an amount of approximately 17 %. The physical properties and grain size of the components can be found in Table 3.

The strength classification of the UHPC was performed based on compressive test results obtained by the participants of the SPP 2020 [4]. The cubic specimens used had lengths of either 100 mm or 150 mm. The UHPC was classified as C130/140 ($f_{cm,cube}$ = 163.9 N/mm^2, measured at 6 cubes with a length of 100 mm). Beyond this classification performed at a concrete age of 28 days, experimental results in [4] showed that for cylindrical specimens (d/h = 60/180 mm) used in the fatigue investigations and cured for more than 90 days, the concrete achieved an average compressive strength of more than 170 MPa.

3. Fatigue investigations and preparation of specimens

The objective of the investigations presented in this paper is to study the damage induced into the concrete's microstructure due to compressive fatigue loading. For this purpose, comparative microstructural investigations were conducted on damaged and undamaged samples of the reference UHPC (named "RU1") within the SPP 2020. This chapter describes the processes used to obtain the samples for the microstructural investigations.

The compressive fatigue investigations in one batch were conducted on cylinders with d/h = 60/180 mm. All specimens were cast in PVC formworks with a casting height of approx. 230 mm. The concrete was filled into the formwork in two layers and each layer was mechanically compacted using a vibrating table. In order to store the concrete under water, the formworks were filled with water immediately after casting. After 48 h of curing, the formworks were removed and the specimens were prepared by sawing a few centimetres of the top and bottom to achieve the final height of 180 mm. Additionally, the surfaces were ground plane-parallel and polished to achieve a uniform stress distribution. Afterwards, the specimens were stored under water at a temperature of 20 °C until reaching the concrete age of 64 days. The specimens were then transferred into a humidity box (20 °C / 95 % min. RH) and stayed there until testing. Therefore, the specimens in this investigations had a high moisture content. The numbering of the specimens includes the number of the formwork and the number of the specimen.

The fatigue reference compressive strength as reference for the calculation of the fatigue stresses was determined in force-controlled tests with a stress velocity of 0.5 MPa/s using five cylindrical specimens with a concrete age of 74 days. The reference specimens were of the same batch, had the same dimensions and storage conditions as those used in the fatigue tests. The mean compressive strength and the standard deviation of the results are shown in Table 4.Table 5

Two types of fatigue tests were performed: tests up to fatigue failure and tests which were stopped at the transition from phase II to phase III of the s-shaped strain development. For both types of tests, the cyclic loading had a sinusoidal wave form with a frequency of f_t = 1 Hz, a minimum stress level of S_{min} = 0.05 and a maximum stress level of S_{max} = 0.75. S is the applied fatigue load over compressive strength. The stress level for this investigation of methods was similar to some other experiments in the priority programme to keep comparability. It results in a high number of cycles until failure and a restricted duration of the tests, to get the number of damaged specimens, necessary for the following investigations. A variation of the stress level was not the aim of the project, but the test of analytical methods. A servo-hydraulic testing machine with a 500 KN actuator was used. In addition to the axial force and the displacement of the actuator, the axial deformations

Table 1
Composition of the reference UHPC ("RU1").

Component	Unit	Quantity
CEM I 52.5 R-SR3 (na) (Holcim Sulfo, Lägerdorf, Germany)	[kg/m^3]	795
Silica fume (Sika® Silicoll P)	[kg/m^3]	169
Quartz powder (Quarzwerke MILLSIL® W12, Frechen, Germany)	[kg/m^3]	198
Quartz sand (0/0.5 mm) (Quarzwerke H33, Haltern, Germany)	[kg/m^3]	971
Superplasticiser (BASF MasterGlenium® ACE 394, Germany)	[kg/m^3]	24
Water	[kg/m^3]	188
w/c$_{eq}$ ratio	[-]	0.19

Table 2
Chemical properties of cement CEM I 52.5 R-SR3 (na).

Materials	Chemical Composition [%]					
	SiO_2	Al_2O_3	Fe_2O_3	CaO	MgO	SO_3
CEM I 52.5 R-SR3 (na)	21.41	3.97	4.79	65.41	0.85	2.98

Table 3
Physical properties and grain size distribution of cement and aggregates.

Materials	Density [kg/dm^3]	Fineness [cm^2/g]	d_{10} [μm]	d_{50}	d_{90}
CEM I 52.5 R-SR3 (na)	3.18	3,969	1.60	11.25	33.18
Quartz powder	2.66	–	2.09	12.71	37.18
Materials	**Density [kg/dm^3]**	**Mass of sieving fraction of total sample [%] 0.063 [mm]**	**0.125 [mm]**	**0.25 [mm]**	**0.5 [mm]**
Quartz sand (0/0.5 mm)	2.65	0	1	44	100

Table 4
Reference compressive strength.

Test	Qty	Concrete age [d]	f_{cm} [MPa]	SD [MPa]
Reference compressive strength	5	74	170.2	3.0

Table 5
UHPC, results of the C-S-H analysis (6 determinations per value).

	Before fatigue loading	After fatigue loading
wt.-% Si in Q^1 in C-S-H	2.0 ± 0.2	2.0 ± 0.1
wt.-% Si in Q^2 in C-S-H	3.1 ± 0.3	3.3 ± 0.2
Sum of two lines above	5.1 ± 0.3	5.3 ± 0.2
Mean chain length C-S-H	5.0 ± 0.5	5.2 ± 0.4

of the specimens were measured continuously using three laser distance sensors positioned on the circumference of the specimen at 0°, 120° and 240° (test set-up is shown in [4]). Furthermore, the temperature of the specimen's surface was measured for the purpose of monitoring. All specimens were tested in a dry environment. The fatigue tests up to failure were conducted on specimens with a concrete age between 74 and 77 days, while the fatigue tests up to phase III were performed on specimens with a concrete age between 80 and 94 days.

First, five specimens were tested until fatigue failure to obtain the s-shaped strain development curves [4]. Based on these curves, a programme was adjusted for the UHPC to automatically stop the test at the transition from phase II to phase III once a threshold value in the gradient of strain increase is exceeded. A total of 14 specimens were fatigue loaded up to the transition between phase II and phase III and, thus, fatigue pre-damaged. With each pre-damaged specimen, a "twin" specimen was treated in exactly the same way (e.g. also placed in the testing machine) but not loaded in order to expose it to exactly the same environmental conditions as the damaged one. After the fatigue tests, the fatigue-damaged and the undamaged twin specimens were stored in sealed plastic bags and stored at a temperature of 20 °C until the preparation of samples for the microstructural investigations. The results of the fatigue tests are shown in Fig. 1.

In Fig. 1, the single and mean values of the numbers of cycles to failure or, rather, the numbers of cycles up to the test stop are shown. It can be seen that the scatter of the single results is quite large, especially for the tests up to the transition between phase II and phase III. The mean number of cycles to failure was $\log N_f = 3.765$ with a standard deviation of 0.304 $\log N_f$. The pre-damaged specimens had a mean number of cycles of $\log N = 4.064$ and a standard deviation of 0.470 $\log N$. The type of the fatigue regime in this test is therefore high cycle fatigue. For the stopped fatigue tests, the strain developments and the pre-damaged specimens themselves were checked in order to examine whether no specimen had stopped too early or late. The circumferential surfaces of seven pre-damaged specimens are shown in Fig. 2 exemplarily for illustration purpose.

From Fig. 2 it is obvious that macro damage had already occurred with spalling of large portions of the shell surface up to the test stop in each case.

In the last step, the samples for the microstructural investigations were cut from pre-damaged and the undamaged twin specimens and afterwards sent to the research partners. Most of the research partners required disc-shaped samples of the material obtained from the central part of the cylindrical specimens with height of 5, 10, 20, 35 or 75 mm. In addition, vertical slices were required also from the central part of the cylinders with a thickness of 10 mm. Examples of the cutting pattern are shown in Fig. 3.

The specimens were wet cut with a conventional stone saw. After cutting, the samples were sealed in plastic bags and sent to the research partners in shockproof boxes for the microstructural investigations. The concrete age of the samples at shipping day was 98 days.

4. Methods and results

A series of methods was used to characterize the UHPC and the effects of the compressive fatigue loading. Principles, references, advantages, restrictions and important results are reported in the following. Fig. 4 shows the methods and their spatial resolution.

4.1. Light microscopy

The chapter is focused on polarized light microscopy, which is a very powerful technique to analyze the structure and phase composition of specimens with a resolution down to some micrometers. Often specimens are examined in transmission of thin sections with a thickness of about 30 μm, although reflected light, powder and suspensions can be used as well. Phases are identified by their crystal shape, color, the change of color by rotating the thin section, the refractive index, the splitting behaviour and typical reactions. With crossed polars the birefrigence and the behaviour by rotating (extinction) can be used as well. Changes in porosity are observable by the change of color-intensity, if a colored resin is used to prepare thin sections. The so called conoscopic technique gives additional information on the crystal structure of the grain in the focus, but is restricted to crystals larger than 60 μm. Details are beyond the scope of this paper and readers are refered to [7,8] for the analytical technique and [9] for the application in civil engineering.

The UHPC before and after compressive fatigue loading was examined as thin sections. Fig. 5 shows a low magnification overwiew on the not loaded (pristine) UHPC. Only the large grains of the aggregate are resolved. Most of the grains are quartz, with some minor amounts of other minerals resp. rock types. It is visible in the picture made with crossed polars that most of the grains are single crystals and only a few grains are polymineralic. Some of the quartz grains show undulose extinction, indicating an oriented stress during the history of the material. The size and shape of the grains can be determined.

With high magnification, quartz powder and parts of the binder are resolved (see Fig. 6). Most of the grains in the binder with sharp

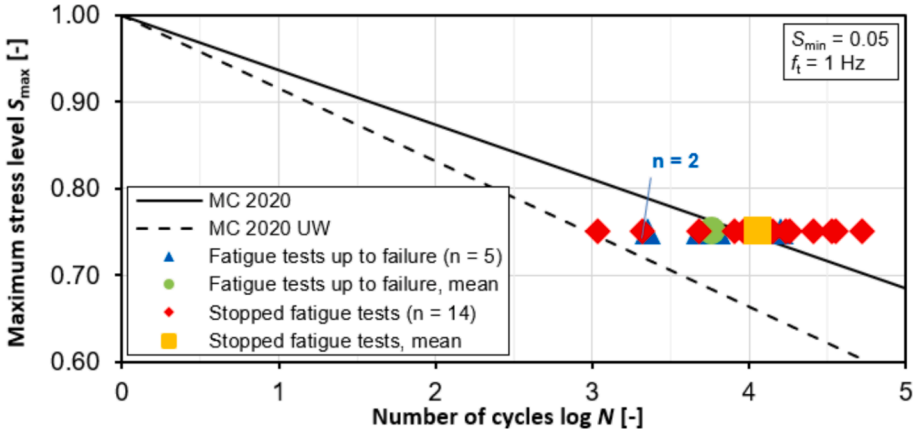

Fig. 1. Numbers of cycles to failure or, rather, up to test stop of the UHPC specimens.

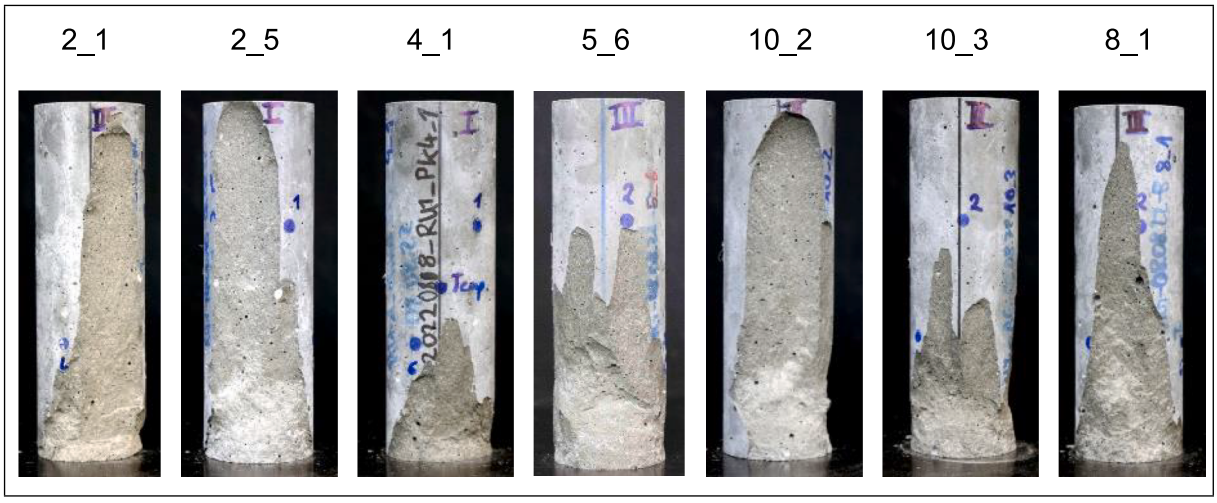

Fig. 2. Circumferential surfaces of seven pre-damaged specimens (exemplarily). Specimens stopped at the transition of phase II to phase III.

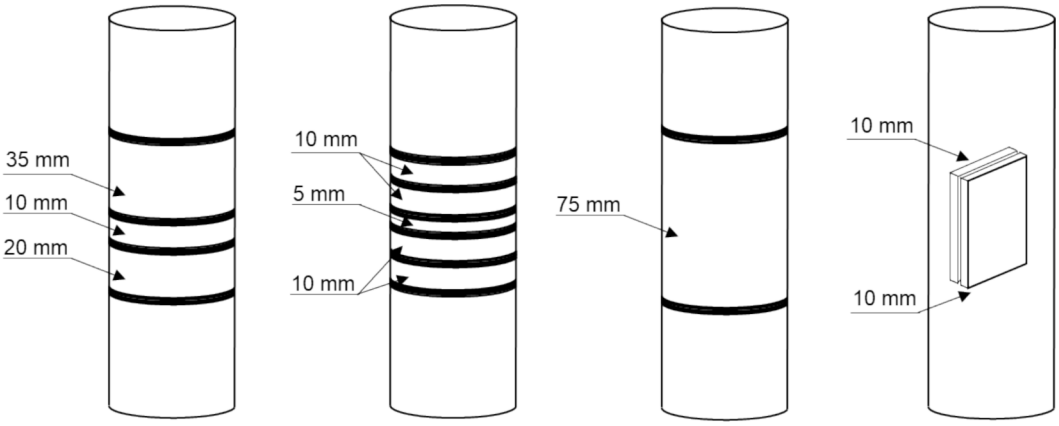

Fig. 3. Example of cutting pattern.

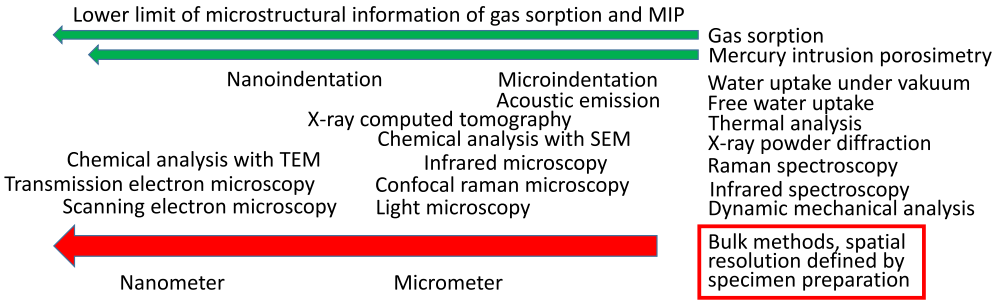

Fig. 4. Used methods and their spatial resolution.

boundaries are unreacted C_3S, C_2S and C_4AF. Portlandite is visible by the light color with crossed polars. Calcium-Silicate-Hydrate (C-S-H) is unspecific and can not be resolved with light microscopy. Typical clusters of C_2S and agglomerates of silica fume are visible in very low quantities (see Fig. 7). The primary particles of silica fume are beyond the resolution of a light microscope.

Although this is not provable, it seems, that the number of cracks in the UHPC specimens after fatigue loading is higher than before. The visible cracks are some micrometers long and less than one micrometer wide (see Fig. 8). They can be best seen with crossed polars by the scattering effect, because the field with crossed polars is quite dark. There is a danger of confusion with portlandite and the Becke line, a bright line at grain boundaries. An increase in quantity of cracks due to fatigue loading was also found for the high-strength (reference) concrete (HPC) within the priority programme, see [10,11] for further details. In HPC, the typical crack width is larger. In [12], an increase of cracks by fatigue of HPC is also observed, especially near the aggregate grains. In addition, light microscopy can also be used for the investigation of many other aspects, for example inclined fiber pullout, see [13].

4.2. Electron microscopy (SEM, TEM)

Electron microscopy has proven to be a powerful tool for the investigation of cementitious building materials. Over the course of the past

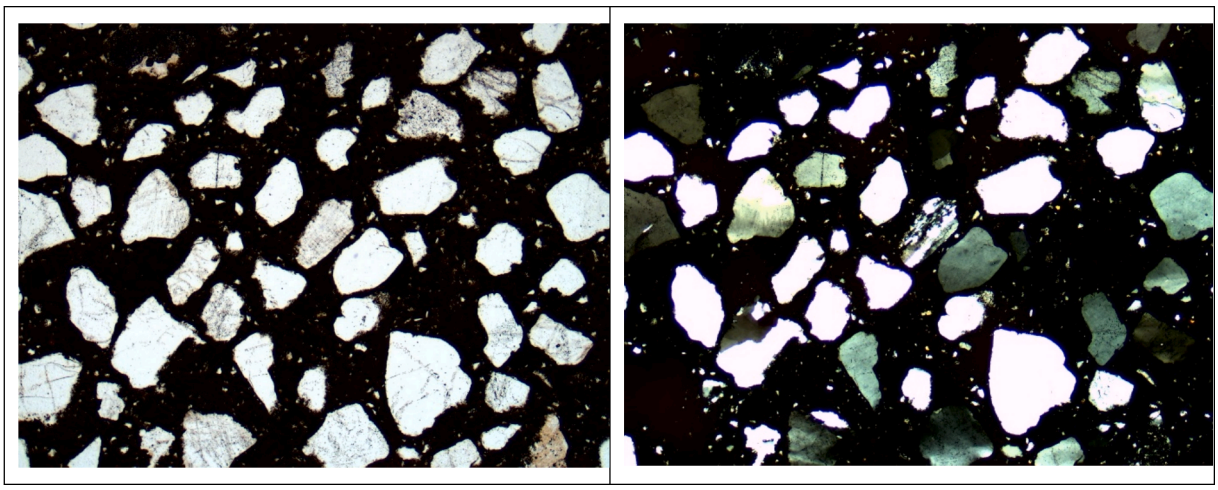

Fig. 5. Thin section, pristine UHPC, picture width 2.45 mm, overview, left without, right with crossed polars. Several quartz grains in matrix.

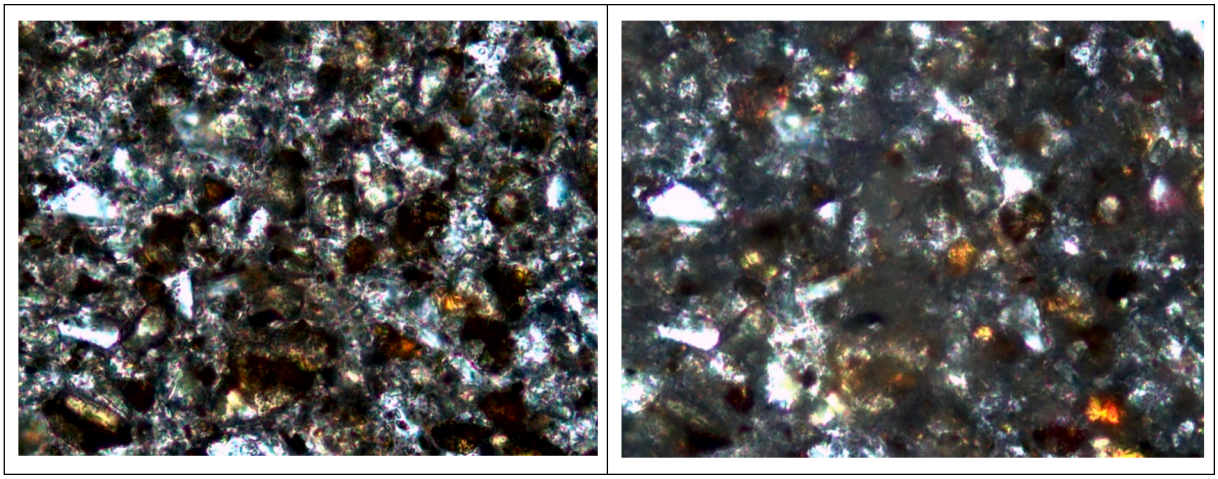

Fig. 6. Thin section, pristine UHPC, picture width 0.16 mm, left without crossed polars, right with crossed polars. Binder matrix with quartz powder.

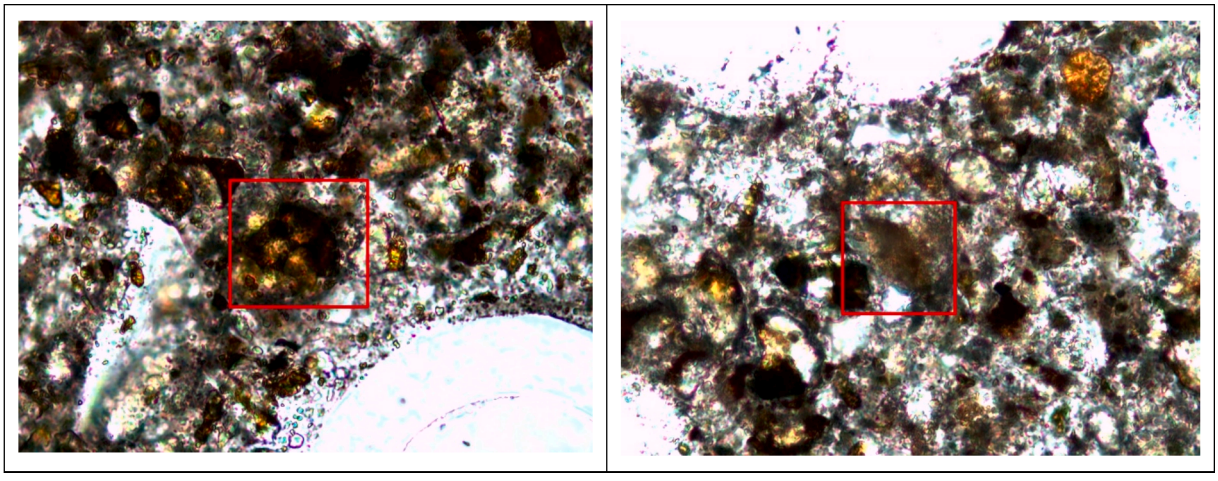

Fig. 7. Thin section, pristine UHPC, picture width 0.16 mm, without crossed polars, left C_2S cluster, right silica fume agglomerate (in squares).

decades, scanning electron microscopy has been employed for the analysis of cracks [14], porosity [15] and composition of cement paste [16]. To characterize specific hydration products in the cement paste matrix on a micrometer or nanometer scale, scanning (SEM) [17] and transmission electron microscopy (TEM) [18], respectively, have been commonly applied.

Regardless of the excellent spatial resolution and chemical analysis capabilities that electron microscopy provides, a few drawbacks should

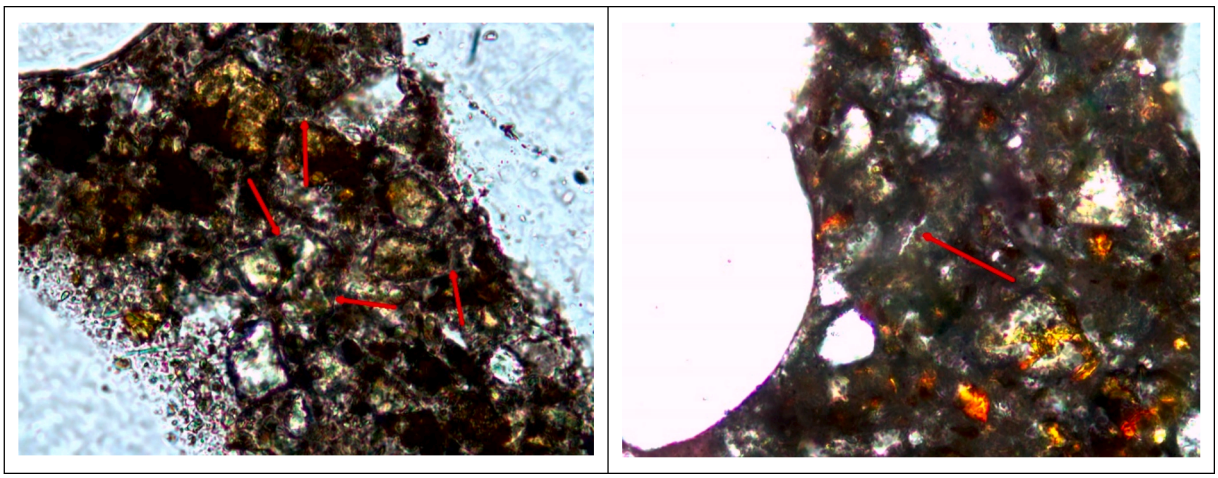

Fig. 8. Thin section, UHPC after fatigue loading, picture width 0.16 mm. Left without crossed polars, arrows to possible cracks, but uncertain because of possible confusion with the Becke line. Right different region with crossed polars, the crack (arrow) is well visible.

be taken into account. Unless environmental SEM is employed [19], investigations take place in high vacuum, causing considerable shrinkage in cementitious materials [20]. The necessity for ultrathin samples in TEM requires specialized experimental setups or sophisticated preparation techniques such as focused ion beam (FIB).

Here, automated large-area SEM with backscattered electron imaging (BSE) on finely ground UHPC surfaces were used for preliminary compositional analyses and to find suitable sites for the FIB sample preparation. Quartz aggregate, cement paste and unhydrated clinker grains can be easily distinguished based on their respective dark, medium and bright atomic number contrasts (see Fig. 9).

For TEM, ultrathin FIB-prepared lamellae crossing the interface of aggregate and cement paste were extracted. Using high-angle annular dark-field (HAADF) imaging with atomic number contrast, microstructural changes in the cement paste matrix with increasing fatigue damage were observed.

In pristine samples, C-S-H phases with a finely fibrous morphology are found, as it is known from literature. From the early onset of fatigue damage, the morphology appears denser, with objects of dark material contrast forming in the cement paste matrix. These precipitates exhibit an elongated shape with a length of around 200 nm and a width of around 20 to 50 nm; they do not grow in size as fatigue damage progresses, but become more numerous (see Fig. 10). In the samples described in this paper, a small number of precipitates can already be observed in the pristine material.

The darker material contrast of the precipitates indicates a material of lower density and/or a lower average atomic number with respect to the surrounding C-S-H phases. Additionally, many precipitates grow, shrink or disappear entirely upon energy intake due to electron beam irradiation during TEM experiments. EDS (energy dispersive X-ray spectroscopy) elemental mapping shows higher concentrations of aluminum and sulfur in regions of cement paste containing a large number of precipitates or nanocracks.

The chemical composition and the tendency to transform upon energy intake indicate the presence of ettringite, a calcium aluminum sulfate hydroxide mineral. Due to its high content of physically bound water, it has a low density of 1.77 g/cm^3 and can exert high pressure on surrounding materials upon crystallization. A delayed formation of ettringite inside hardened cementitious materials can be detrimental to the long-term stability of building components. A change of number or size of ettringite crystals can exert pressure and, thus, mechanical stress on the surrounding material, i.e. the C-S-H phases and therefore can be a source of nanocracks. Characterizing ettringite formation on a submicrometer scale would have proven difficult or impossible using

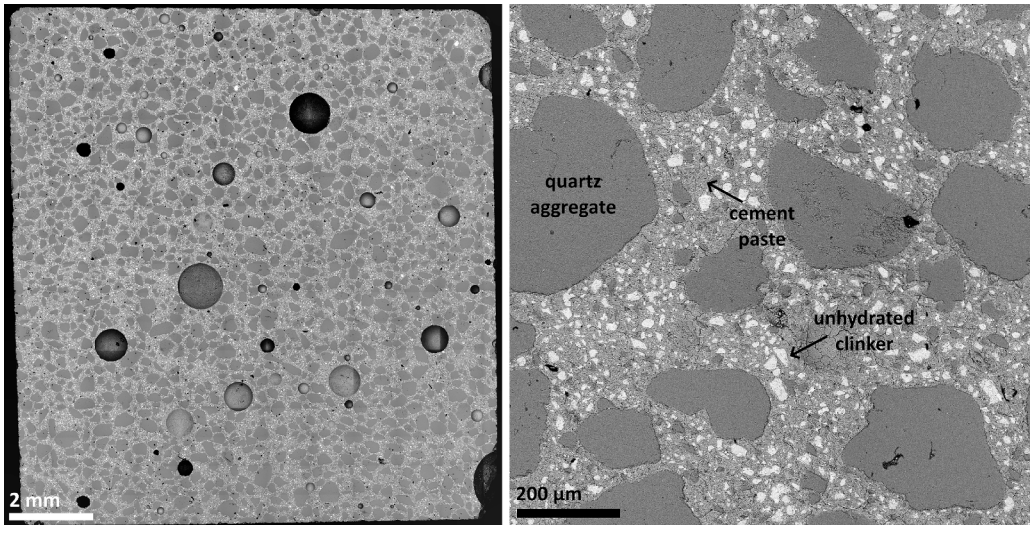

Fig. 9. Large-area (sample surface ca. 1 cm^2) and detailed BSE-SEM images of pristine UHPC. Quartz aggregate, cement paste and unhydrated cement clinker appear dark, medium and light grey, respectively.

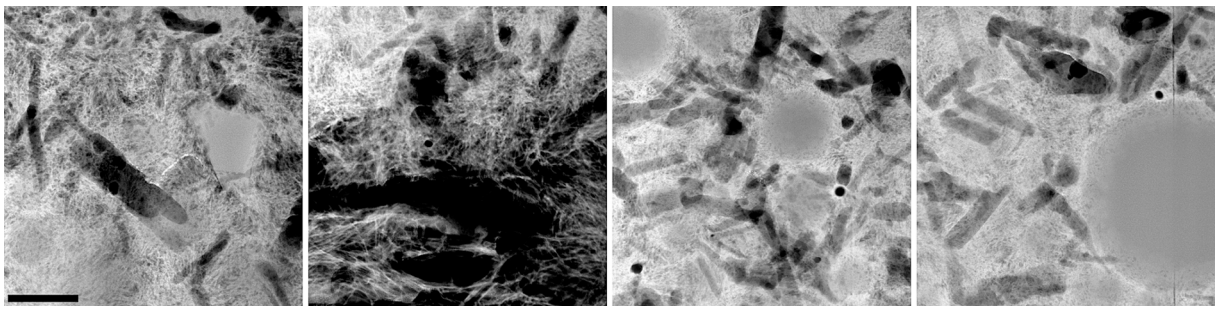

Fig. 10. HAADF-TEM micrographs of microstructural changes in UHPC cement paste. Left two images: pristine material; right two images: after fatigue loading. Scale marker is 200 nm for all images.

methods other than electron microscopy.

4.3. Infrared spectroscopy (IR)

Infrared spectroscopy is based on the stimulation of molecular vibrations and rotations in the specimen. The absorption is very characteristic, but only movements, resulting in a change of the dipole moment yield an IR absorption. Gases, liquids and solids (crystalline and amorphous) can be analyzed. For detailed information on IR spectroscopy see [21]. IR transparent materials can be analyzed in transmission.

The investigation was performed with a Perkin Elmer Spectrum Two instrument by attenuated total reflection (ATR)-IR spectroscopy ([22]). The powder was pressed on a single reflection diamond ATR. The interaction of the generated evanescent wave with the specimen results in the ATR-IR-spectrum. This spectrum is not equal to a conventional IR spectrum, but convertible. Fig. 11 shows the spectra of the UHPC after the conversion into a conventional IR spectrum. The peaks at the low end of the spectra are mainly generated by unhydrated cement phases. The double peak around 800 cm^{-1} results from quartz. The following broad peak is an overlay of many peaks described further below. All differences between the samples before and after fatigue loading outside this group can be explained by small variations of the binder-quartz-ratio and are not a consequence of the fatigue loading. The peak around 1420 cm^{-1} is generated by carbonation, the peaks at 1640 and 3400 cm^{-1} by water, the sharp peak at 3640 cm^{-1} by portlandite and the double peak at 2120 cm^{-1} by potassium ferricyanide, used as internal standard.

Fig. 12 shows one of the peak fits in the region of the broad peak around 1000 cm^{-1}, mainly generated by the silicate species. The peak fit was done with the software „Peakfit“. It is impossible to separate the signals without a detailed knowledge of the individual species present in the sample and their peaks. An automatic fit is impossible. The Q^1 signal from C-S-H is at 840 cm^{-1}, the Q^2-signals at 957 and 1006 cm^{-1}. The other peaks resulted from unhydrated cement (875, 914), quartz (775, 798, 1055, 1088, 1165), sulfate (1117) and unreacted silica fume. The signals of quartz cannot be distinguished from unhydrated silica fume.

The C-S-H phase was quantitatively determined by the method described in [23], using the Q^1 and Q^2 signals from the C-S-H chains. The results of the investigation are shown in table 5. Although not statistical significant it seems that fatigue loading results both in an increase of the total amount of C-S-H by further hydration, as well as in an increase of the mean chain length of the C-S-H. This can be an effect of temperature increase during fatigue loading. As to be expected, no other systematic difference is shown between samples before and after fatigue loading.

4.4. Raman spectroscopy

Raman spectroscopy is a non-destructive analysis method that provides information about the vibrational and rotational states of molecules or groups of atoms, similar to IR spectroscopy (see Chapter 4.3). In contrast to IR spectroscopy, Raman spectroscopy records the periodic changes in polarizability caused by molecular vibrations and not those of the dipole moments.

The findings of the interaction between irradiated light and matter provide information about the bonding states of the material being analysed. A monochromatic light (laser) is generally used as the

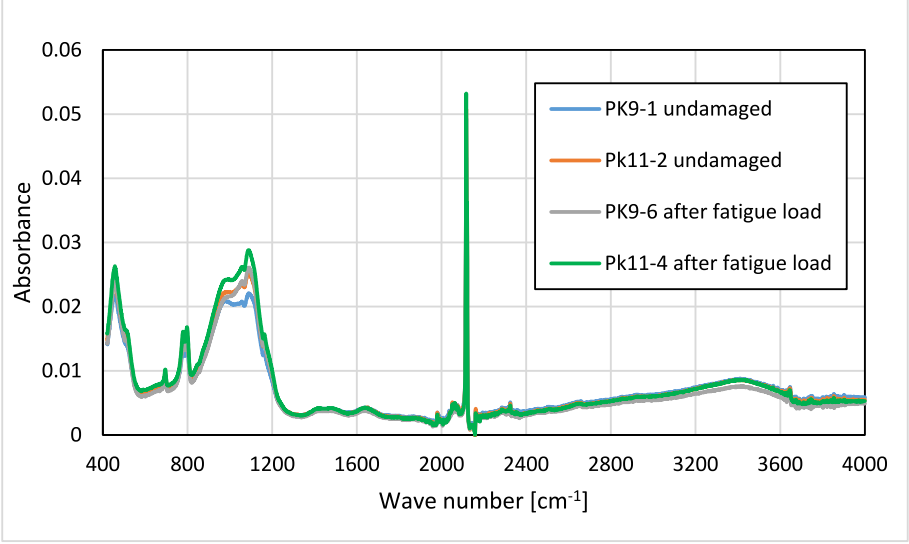

Fig. 11. UHPC, ATR-IR spectra after ATR conversion, peaks see text.

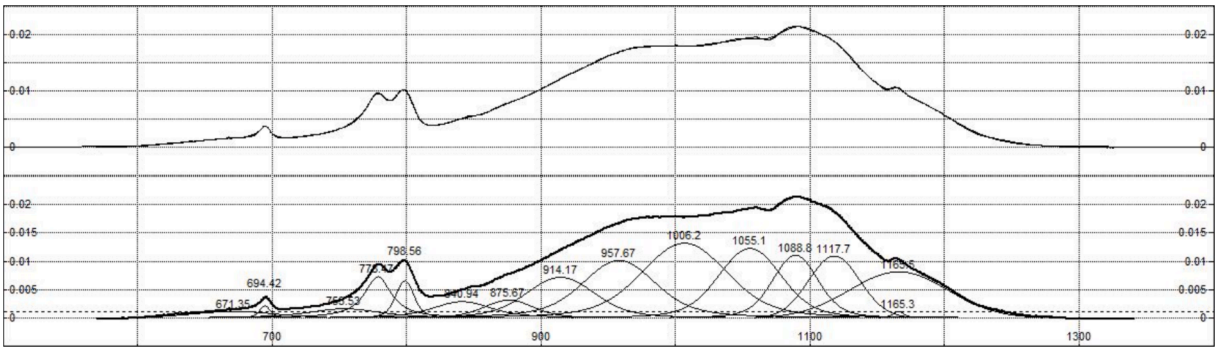

Fig. 12. UHPC without fatigue loading, peak fit in the region around 1000 cm^{-1}, peaks see text.

excitation source. While most of the laser light passes through the sample, a small proportion of the absorbed energy with the frequency of the laser light is scattered elastically in all directions (Rayleigh scattering) and an even smaller proportion is scattered inelastically by the sample (Raman scattering or Raman effect).

For the investigations of the fatigue-damaged and undamaged reference UHPC samples, confocal Raman microscopy (CRM) was used to couple spectral information with image based phase position. For further information about confocal Raman microscopy and Raman spectroscopy, in general the reader is referred to [24].

The disc-type sample slices (two undamaged reference samples and two fatigue-damaged samples) with the dimensions $d/h = 60/35$ mm were further prepared after wet sawing (see chapter 3). For CRM investigations, the surface roughness should be as smooth as possibly to reduce topographic influences on the spectroscopic results. Therefore, a polishing procedure with different SiC abrasive papers was performed. The polished discs were stored at 33 % relative humidity and under N_2 atmosphere until testing. Large area scans of 1500 x 1500 µm (100 lines x 100 points) – so-called 'Raman Mapping' – were performed on a confocal Raman microscope (Alpha 300RA from Witec, Germany) using a laser with 532 nm wavelength for excitation. The spectra were recorded using a 20x magnification objective (0.5 N.A.), a continuous laser beam, a grating of 600 g/mm, an integration time of 3 s and 3 accumulations per spectrum.

Fig. 13 represents a combination of a microscope image (4 mm x 4 mm) with an overlayed Raman mapping (1500 µm x 1500 µm) and corresponding spectra. Clearly visible in the spectra some of the starting materials can be rediscovered. The sharp and strong symmetric stretching modes of Si-O-Si at 464 cm^{-1} along with medium intensity lattice vibration modes around 205 cm^{-1} and a number of weak bands (Fig. 13 – red spectrum) derives from quartz sand and crystalline quartz powder (SiO_2) addition of the concrete mix.

The left microscope image in Fig. 13 shows that the investigated UHPC has a high packing density and that a large proportion of the particles visible on mm-scale can be assigned to quartz sand (red particles). The clinker phases of the added cement are still visible as strong and sharp bands around 852 cm^{-1} and broader bands around 977 cm^{-1} which are assigned to the symmetric stretching and asymmetric stretching mode of Si-O in C_2S respectively (Fig. 13 – blue spectrum). An asymmetric broadened peak with a high Full Width at Half Maximum (FWHM) around 719 cm^{-1} represents remnants of C_4AF.

Bands in the 770–796 cm^{-1} region can be attributed to silicon carbide originated mainly from the SiC-abrasive paper in the course of sample preparation and to a small extent from the silica fume addition of the concrete mix.

In addition to the starting materials, the hydration products which are formed during hydration of the cement can further be identified in the Raman spectra. From the overlayed Raman mapping in Fig. 13, particles (green), which are significantly smaller than the quartz sand particles – on the illustrated mm-scale – are clearly visible. Despite having a lower proportion in the matrix, they are regularly distributed and can be clearly recognised as an independent phase. Based on the corresponding spectra, these phases can be identified as portlandite by the lattice vibration (Ca-O) around 357 cm^{-1} and OH-stretching vibration of the hydroxyl group (Ca-OH) around 3616 cm^{-1}. Intermixed with the spectrum (green) of portlandite, another hydration product can be identified by a weak broad shoulder around 660–680 cm^{-1} and can be attributed to bending vibrations of Si-O-Si from the formed calcium

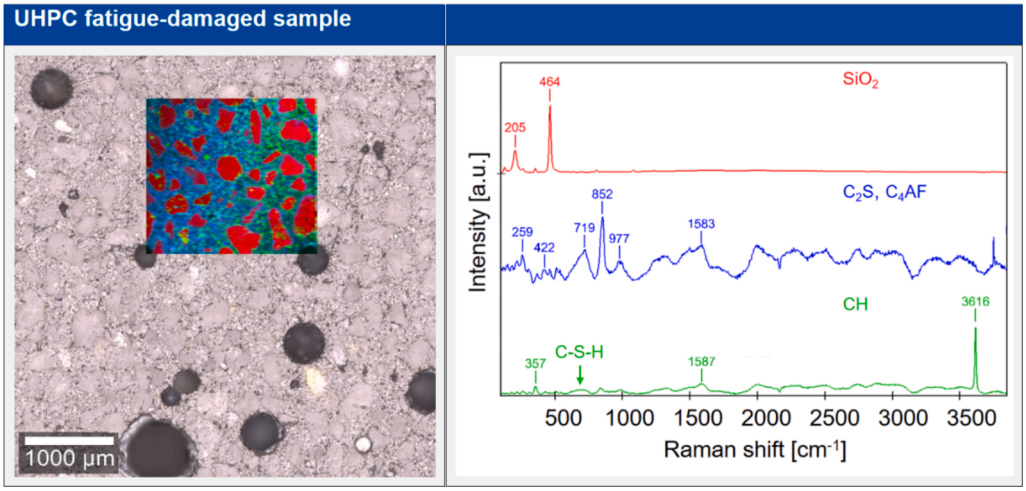

Fig. 13. Raman mapping and correlated spectra of a fatigue-loaded UHPC sample. Microscopic image with Raman mapping overlay (left) and attributed spectra (right).

silicate hydrate (C-S-H) [25]. A slight gradient in the Raman mapping image is due to topographic inhomogeneity due to sample preparation.

Ettringite and monosulfate as hydration products from gypsum are contained in all samples and can be identified by symmetric stretching vibration of SO_4^{2-} around 990 cm^{-1} (not shown here). Moreover a Raman shift around 1086 cm^{-1} (not shown here) can be attributed to the symmetrical stretching of CO_3^{2-} of calcium carbonate (mostly calcite) and is present in all samples. The broad bands around 1583–1587 cm^{-1} are stretching vibrations of carbon, which derives most likely from the tools of the milling procedure of the raw materials.

Comparative analyses of the undamaged reference samples and the fatigue-damaged samples of the UHPC did not reveal any clear differences that would indicate a change in the structure due to fatigue loading. Nevertheless, Raman microscopy is a helpful, non-destructive analytical method for phase identification and imaging phase localisation.

4.5. X-ray powder diffraction (XRD)

Crystalline structures exhibit distinct diffraction patterns when exposed to X-ray radiation. By analyzing these powder diffraction patterns, valuable information about the material's crystal structure, including lattice constants, lattice types, crystallite sizes, phase identification, and microstructural properties, can be obtained. In contrast, amorphous materials lack well-defined diffraction peaks and instead display a continuous background signal without discernible diffraction maxima. This characteristic background signal provides insights into the structural parameters and changes of existing amorphous phases [26]. The diffraction of X-rays adheres to Bragg's law [27], which states that diffraction occurs only when the angle of incidence matches the angle of reflection, satisfying the diffraction condition

$$n\lambda = 2d \cdot sin(\theta) \quad (1)$$

In this equation, λ represents the wavelength of the X-rays, d signifies the spacing between lattice planes, n is a constant and θ denotes the diffraction angle.

The measurements were conducted using a Philips ẊPert Pro unit with Bragg-Brentano geometry. A Cu-tube was utilized, operating at 40 kV and 30 mA. A progressive divergence and receiving slit with a 20 mm irradiated length were utilized. The sample was ground without drying and prepared with a back-loading system. The measurement range of 3-70° 2ϑ was scanned with a step size of 0,02° and a measuring time of 1 s per step.

The analysis of the generated powder data was performed through qualitative phase identification. This approach entails comparing the experimental powder diffraction pattern with reference databases containing characteristic diffraction patterns of numerous well-known materials. By aligning the measured diffraction peaks with those in the reference databases, phases present in the analyzed powder can be identified.

Other evaluation methods include quantitative phase analysis using the Rietveld method or least-squares fit analysis. These techniques involve mathematical calculations to determine the percentage of individual phases in the mixture. Additionally, lattice parameters can be determined by indexing the diffraction peaks, and crystallite sizes can be estimated based on the shapes of the diffraction profiles. Furthermore, texture analysis can be conducted by examining the distribution of intensities of the diffraction peaks as a function of the diffraction angle. Further literature on X-ray (powder-)diffraction can be found, for example, in [28–30]. The application to problems of civil engineering is described in [31].

Crystalline phases identified in UHPC powder include quartz, C_3S (alite), C_2S (belite, larnite), C_4AF (brownmillerite), portlandite and ettringite (see Fig. 14). The broadened peak observed at around 29° 2θ is ascribed to X-ray amorphous C-S-H phases [32,33] and unreacted silica fume [34], respectively. However, due to peak overlap, it is not possible to conclusively determine whether calcite has formed as a result of carbonation. The intensity, peak positions and peak shapes of specimens before and after fatigue loading were meticulously compared. The only discernible differences were attributed to slight variations in the content of unreacted C_3S, C_2S and C_4AF. All diffractograms exhibited a high degree of similarity to the one depicted in Fig. 14.

4.6. Thermogravimetric analysis (TGA)

This chapter focuses on the possibilities of distinguishing between undamaged and fatigue damaged UHPC specimen using thermogravimetric analysis (TGA). According to [35], hydrated cementitious materials should not be ground before analysis, as it may lead to the destruction of hydrate phases. Therefore, our focus is laid on the results obtained from measuring monolithic (moli) samples. In this study, the general drying preparation method of [36] was attempted to apply and

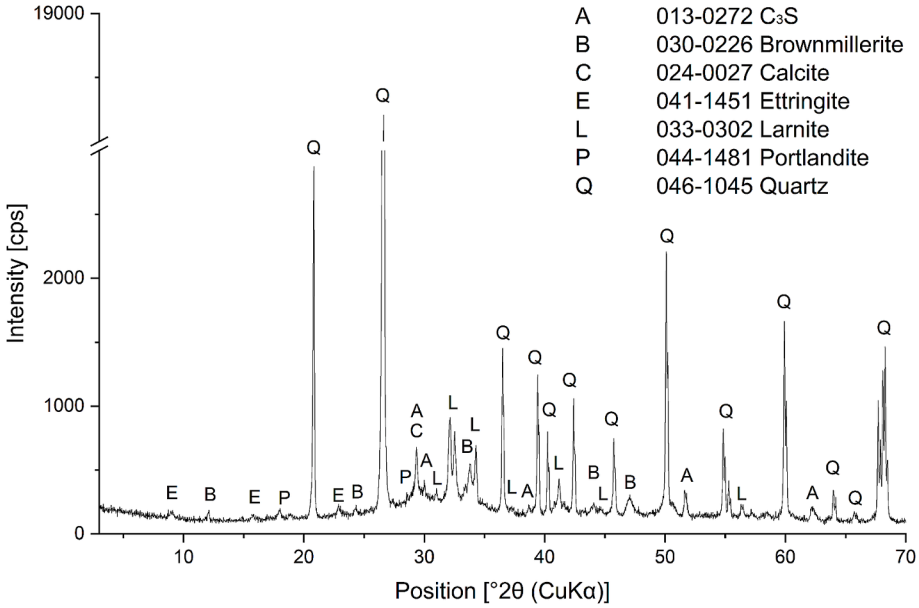

Fig. 14. UHPC after fatigue loading, X-ray diffraction analysis, Cu-radiation. 013–0272 is C_3S with realistic trace element content.

combined with special TGA measurement methods and long-time isotherms. The latter approach, as well as measurements on powder samples (pow) can be found in the Online Resource 1.

TGA is a technique used to measure the change in mass of a sample as it is subjected to controlled heating. This method allows to study a wide range of materials and their properties, such as thermal stability, kinetics, composition, and decomposition. The resolution of TGA signals primarily depends on the heating rate and the sample weight. When the heating rate or sample weight is too high, it can be challenging to distinguish between different weight changes (w-change) occurring at close decomposition temperatures. To address this issue, one option is the use of high-resolution (H-R) TGA, a technique developed by TA Instruments™ [37,38]. In high-resolution TGA, depending on the change in weight, the TGA furnace either maintains a constant temperature or reduces it until no further weight change is observed. Afterward, the furnace resumes heating again.

TGA measurements were performed using a Q5500 from TA Instruments™. To ensure a clear separation of different decomposition temperatures of different materials, the sensitivity value and the resolution number must be set. These two unitless parameters of the H-R method must be adjusted according to the measurement task. The resolution number (−4) represents a specific %/minute weight change, while the sensitivity value (3) is used to minimize temperature overshoot and heater control fluctuation.

Differences between the undamaged and fatigue-damaged samples are hypothesized to result from a potential equilibrium shift or alteration of cementitious UHPC phases. These discrepancies are expected to be reflected in the crystal water content, which may be bound to varying degrees and can be separated using TGA. To remove surface-bounded water, two strategies were followed – isopropanol/diethyl ether treatment (treat) [36] and continuous nitrogen gas flow (latter approach see Online Resource 1: I-T; besides measurements on not-treated (n-treat) specimens).

The discs-shaped specimens within this interlaboratory test were stored in a desiccator with supersaturated sodium bromide solution at the bottom, creating a controlled relative humidity of 58 ± 2 %. As the specimens were sent in wet packaged condition (see chapter 3), the relative humidity declined inside of the desiccator for three weeks until the equilibrium of 58 ± 2 % was reached. Subsequently, thin bars were sawed out of the specimens using a “Buehler IsoMet” low speed saw (Buehler Ltd., Lake Bluff, IL, USA) equipped with a diamond saw blade at very slow speed to minimize further energy input. These thin bars were then further processed by crushing them within a mortar, resulting in the creation of smaller monoliths with a weight of approximately 25 – 32 mg. For the dried samples, both the fatigue damaged samples (9.6_fat_moli_H-R_treat) and the undamaged samples (9.1_n-fat_moli_H-R_treat) were pre-treated with 8 ml anhydrous isopropanol (15 min in 100 ml isopropanol (99,97 % VWR™, dried with 20 g calcium sulfate hemihydrate within 100 ml isopropanol) (Acros Organics™)) to remove surface-bounded water. In a second step the excess of isopropanol was removed by washing with 8 ml dry diethyl ether for 5 min, whereby the diethyl ether treated samples were dried in a drying furnace for 10 min at 40 °C [36]. The non-treated (see Online Resource 1) and dried monolithic samples were measured three times using the H-R method to demonstrate reproducibility.

In general, four different mass losses were observed, the primary step at 50—300 °C can be attributed to the evaporation of water content. The second step observed at 425 °C corresponds to the decomposition of

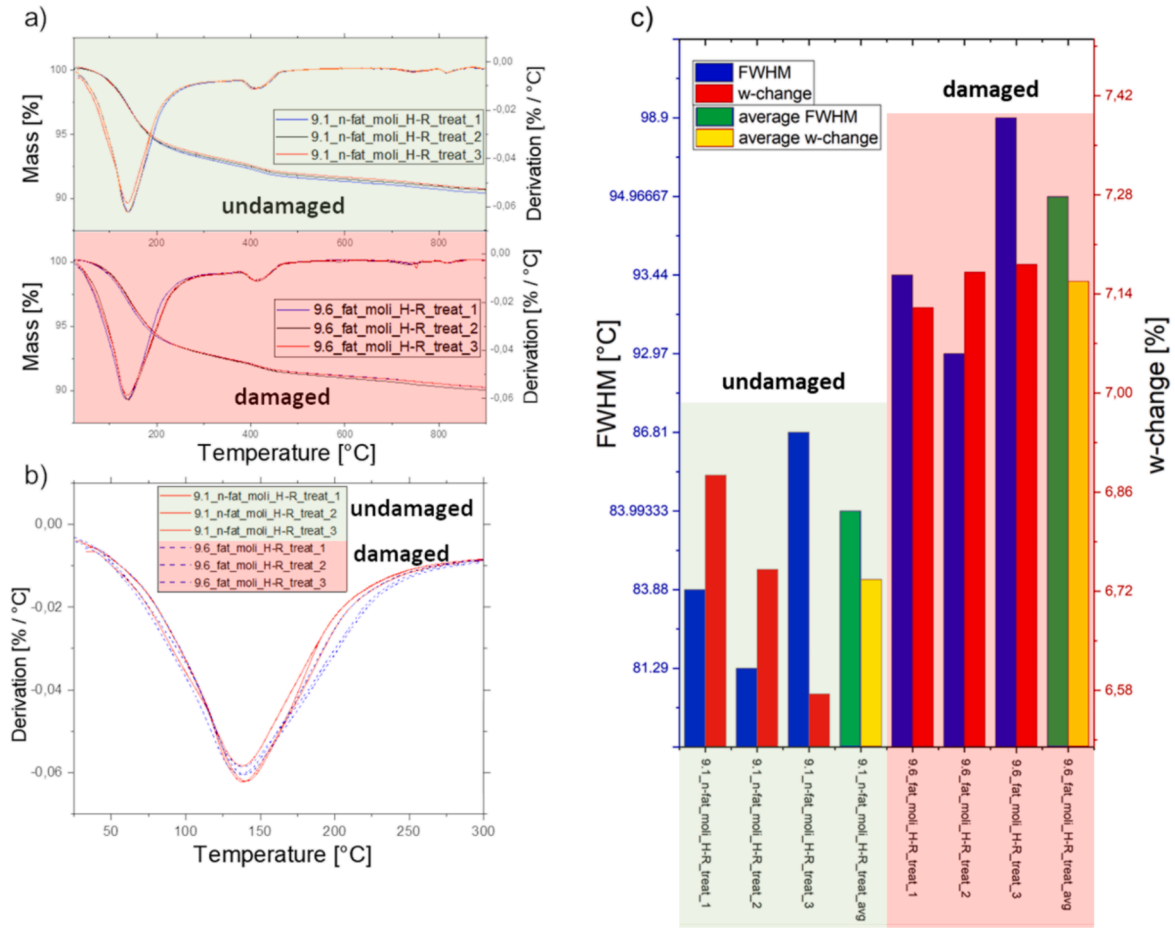

Fig. 15. Mass loss of damaged and undamaged specimens and their derivation a), closer plotted from 30 to 300 °C b) and the FWHM and w-change data c).

calcium hydroxide. At higher temperatures the decomposition of carbonates dominates. According to literature, the decomposition of weakly bonded crystal water in hydrated cement paste finishes in the vicinity of 250 °C [36,39,40]. Consequently, the analysis focused on temperatures up to 300 °C to capture the mass changes and their derivatives accurately using "Trios" software from "TA-Instruments".

Fig. 15 a) shows a comparison of the fatigue damaged and undamaged samples. A direct comparison of the derivations of the mass loss (Fig. 15 b)) in the range from 30 to 300 °C reveals a significant broadening of the Full-Width at Half Maximum (FWHM) at 200 °C. Fig. 15 c) shows a bar graph of each sample, with the averages in mass loss (yellow) and the FWHM of its derivation (green) of the fatigue damaged and undamaged samples. The average FWHM of fatigue damaged samples is about 11.6 % broader than that of the undamaged samples. Fatigued samples also show an average higher mass change of 5.9 %.

The results obtained from the H-R method allow to distinguish between fatigue damaged and undamaged samples. The weight loss and the FWHM of the fatigue damaged samples are significantly higher compared to the undamaged samples. One plausible explanation for this observation is a formation or alteration of the C-S-H phases. On the other hand, the samples were stored in water for further 56 days after mechanical testing and the presence of fatigue cracks could be responsible for further hydration of non-hydrated clinker phase, since the UHPC specimens were made with a low water/cement ratio.

Despite employing the high-resolution (H-R) method, peak separation for monolithic samples proved to be challenging. A pre-drying of the samples showed a better reproducibility and is therefore highly recommended. Additionally, an alternative drying approach in a N_2 gas flow over 48 h, also showed no peak separation (see Online Resource 1: I-T). One possible reason for this issue is certainly a temperature gradient within the samples which led to an undesirable broadening of possible different mass losses, and, thus prevents a peak separation.

Only grinded samples of the undamaged UHPC showed an additional peak at 60 and 80 °C (see Online Resource 1: 9.1_n-fat_pow_H-R_n-treat and 9.6_fat_pow_H-R_n-treat) when analyzed using the H-R method. However, this kind of preparation is not recommended because hydrate phases could be destroyed according to literature [35].

Finally, the recommendation for future investigations is, to use TGA methods directly after fatigue loading to determine, whether or not the observed changes are results of the storage in water or the fatigue loading.

4.7. X-ray computed tomography (XCT)

X-ray computed tomography is an imaging method for non-destructive material testing and three-dimensional visualisation of the internal structure of an object. A conical X-ray beam radiate through a central positioned test object and the intensity of the attenuated X-ray photons are measured by an X-ray detector, which results in a stack of projection images with different grey values. These grey values correlate with the atomic number of the investigated material whereby darker grey values in the projection images represent a higher transmission or lower atomic number than the brighter grey values. In addition to the grey values, the material composition of the test object determine to a not inconsiderable extent the resolution of the projection images. Other factors are the geometry of the test object and device-specific measurement parameters. For further information about theoretical XCT basics, the reader is referred to [41–43] for the associated analysis of the tomographic datasets like reconstruction or further image stack processing.

The fatigue-damaged UHPC samples as well as the undamaged reference samples were investigated with XCT to identify and visualize potential microstructural changes from the loading process. From each of the cylindrical sample slices (three unloaded samples and three fatigue-loaded sample) with the dimensions $d/h = 60/35$ mm (see chapter 3), three cylindrical subsamples with the dimensions $d/h = 10/20$ mm were prepared in the form of drill cores. The undamaged as well as the fatigue-damaged UHPC samples were investigated with a laboratory submicron X-ray computer tomograph (Zeiss Xradia Versa 410) equipped with a sealed 150 kV microfocus X-ray source (continuous operation mode and tungsten reflection target). All tomographic scans were carried out with an acceleration voltage between 80 and 100 kV and tube currents between 100 and 125 μA resulting all in a focal spot size of 7 μm. A quartz glass filter (LE05, Zeiss, Pleasanton, California) was used to optimize the polychromatic wavelengths for an optimal contrast. First of all each sample were measured with a large field low-resolution overview scan to determine regions of interest (ROIs), where microstructural details appear. Higher resolution tomographies for the same field of view (FOV) over the entire sample height could additionally achieved by a vertical stitch procedure, in detail by collecting and stitching of three reconstructed volumes in the vertical direction. Once ROIs are identified, they were further investigated by high-resolution interior tomography scans to get insight into microstructural details of the UHPC samples.

Based on the geometrical magnification – which results from the ratio of the focus detector distance to the focus object distance (FDD/FOD) – and the additional optical magnification different levels of detail of the cement or concrete microstructure can be analysed. For the overview and detail scans of the UHPC samples the different used geometrical as well as optical magnification resulted in a pixel resolution of the images in the range 0.96 px to 10.85 px (see Fig. 16 and Table 6). A pixel binning of 2 x 2, an exposure time of 3/12/70 s per step and a total of 3201 projections over a 360° rotation resulted in large data sets (comp. Table 6), which were subsequently reconstructed. The 3D-tomographic reconstruction of all scans was done by a filtered back projection method and the Feldkamp-Davis-Kress reconstruction algorithm [43] using the software XMReconstructor (Zeiss). Within the reconstruction, the beam hardening was corrected and the image quality was optimised using a Gaussian filter. The reconstructed tomograms were further processed using Avizo 9.4 (Thermo Fisher Scientific, VSG) to visualize the orthogonal slices as can be seen in Fig. 16.

The basic structures of the UHPC samples are clearly visible in the low-resolution overview images. Four components are directly visible in the tomography images based on their different densities (atomic number): black, predominantly spherical areas indicate the medium and large capillary pores and some air pores, image areas in dark grey represent the aggregates (here quartz sand), the smallest white particles can be assigned to particles with high densities such as iron oxides/titanium oxides or clinker minerals like C_3S, C_2S, C_4AF. The remaining light grey area shows the cement paste matrix with finely distributed hydrate phases, which cannot be resolved with submicron XCT (Fig. 16).

Using an image-processing programme, the individual sectional images and the reconstructed volume were examined more closely. This allows individual localities with elongated defects to be discovered, which could indicate fatigue-induced damage. However, these defects were found to a comparable extent and frequency in the undamaged and fatigue-damaged samples examined. Higher magnifications and higher resolution scans show the position and shape of these defects in greater detail, but were not sufficient for a clear differentiation or allocation of damaged and undamaged areas of the samples, even in the detailed images of these individual examinations.

As a non-destructive imaging method, XCT is generally very well suited to analyzing the (fatigue) damage occurring in concrete; however, the detection of such damage zones at micrometer level in comparably large specimens still poses a major challenge.

4.8. Dynamic mechanical analysis (DMA)

A Dynamic Mechanical Analysis (DMA) setup is presented, which enable the characterization of evolving effective mechanical properties through forced compressive oscillations. The DMA setup allows the direct measurement of harmonic longitudinal and transversal strains

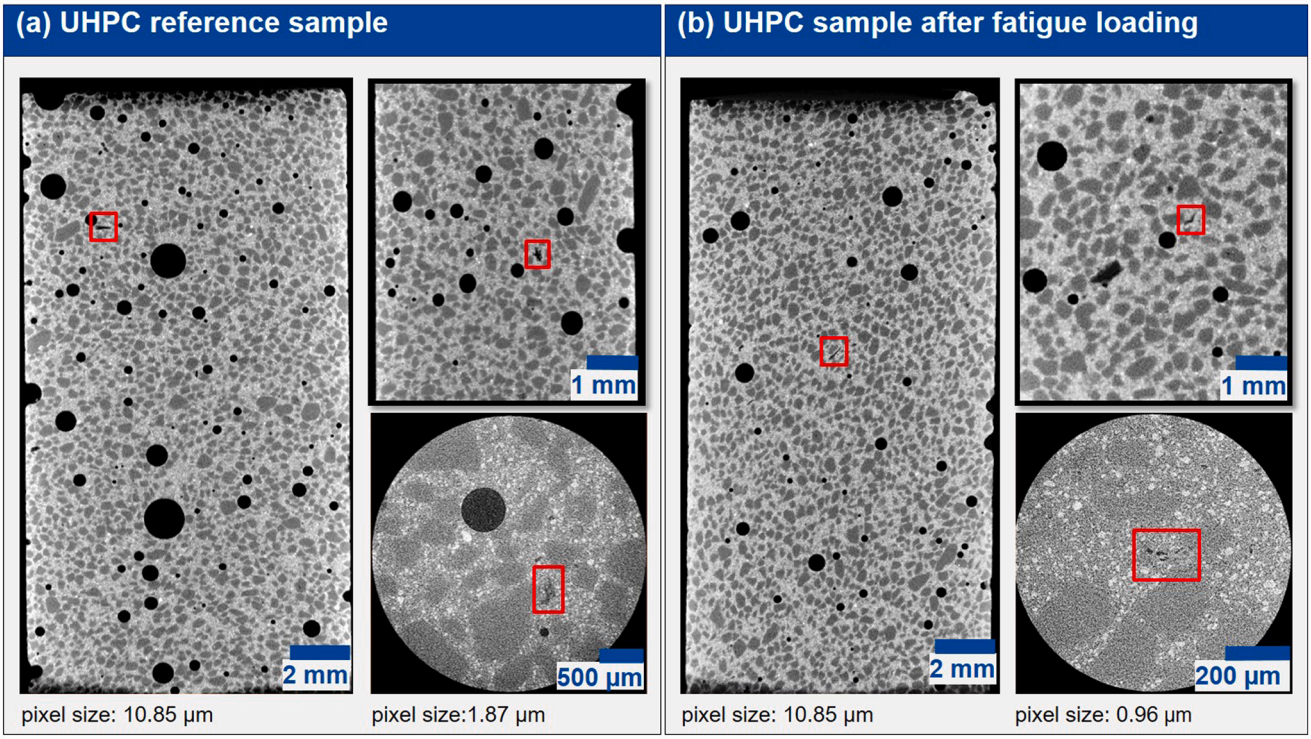

Fig. 16. Large field low-resolution overview scan, vertically stitched (left), zoomed-in (top right) and high-resolution interior tomography scan (bottom right) of (a) an UHPC reference sample before loading (b) an UHPC sample after fatigue loading. Red rectangles mark areas with microstructural features.

Table 6
Experimental parameters for XCT measurements.

	overview scan	detail scan	detail scan
voltage [kV]	80	100	80
tube current [µA]	125	100	125
focal spot size [µm]	7	7	7
focus-detector-distance [mm]	230	58	49
focus-object-distance [mm]	36	18	14
optical magnification	0.4	10.0	20.0
exposure/acquisition time [s]	3	12	70
projections	3201	3201	3201
binning	2	2	2
filter	L05	L05	L05
stitch segments	3	–	–
pixel size [µm]	10,85	1,87	0,96

through strain gauges on the sample, as well as harmonic axial forces. From the sinusoidal strain and force transients, effective properties like the complex Young's modulus and the complex Poisson's ratio can be computed. For compressive harmonic excitations, a high-voltage piezoelectric actuator is used, which could be statically pre-stressed and which allows for applied frequencies up to 1 kHz.

The schematic diagram of the DMA setup is depicted in Fig. 17. The investigated samples have a cylindrical shape (length/diameter = 2.5, with diameter = 30 mm). The DMA setup is subjected to a static preload within a mechanical universal testing machine (Schenk-Trebel RM 50). A frequency generator (Physik Instrumente P-517) generates low amplitude sinusoidal voltage signals (−5 − +5 V) which are amplified through a high-voltage linear amplifier (Physik Instrumente E-482). With a maximum amplification factor of x = 100, the continuous sinusoidal signal is transmitted to the high-voltage piezoelectric actuator (Physik Instrumente P-235.2 s). Using the piezoelectric effect, the actuator converts the high-voltage signal into harmonic forced oscillations with amplitudes of up to 40 µm. A piezoelectric force sensor (HBM CFW/50KN) with high-frequency sensitivity measures the resulting axial force. Additionally, a (redundant) calibrated aluminum cylinder with axial strain gauge is applied to measure the axial force.

For local strain measurements, the cylindrical UHPC sample was equipped with two strain gauges (HBM K-CXY1 T-Rosette). To monitor the temperature in the vicinity of the sample, a PT-1000 temperature sensor was employed. The applied low-frequency signal, the axial force measured in the piezoelectric load cell and in the aluminum standard, the axial and transversal strains, and the temperature of the piezoelectric actuator were recorded using a 24 bit high-speed transient recorder (HBM-HBK GEN2tB and GN1640B). The data transients are post-processed within sliding windows and transformed to frequency domain using a fast Fourier transformation (Matlab, The MathWorks, Inc.). Finally, effective complex mechanical properties ($E(\omega)$ and $\upsilon(\omega)$) are calculated from the raw signals. A detailed discussion of the forced oscillation setup and alternative DMA setups can be found in [44–46].

From the post-processed data, for each excitation frequency (0.1 Hz $< f <$ 1000 Hz) the complex Young's modulus $E(\omega) = E'(\omega) + iE''(\omega)$ and complex Poisson's ratio $\upsilon(\omega) = \upsilon'(\omega) + i\upsilon''(\omega)$ (i is the complex unit) is obtained. The ratio of the loss modulus $E''(\omega)$ and the storage modulus $E'(\omega)$ describes the loss factor $tan\varphi_E = E''/E'$ which characterizes the intrinsic attenuation of the sample. Note that $\varphi_E(\omega)$ is the phase shift between axial stress and axial strain in case of Young's modulus ($E(\omega)$). Regarding complex Poisson's ratio ($\upsilon(\omega)$), the phase angle $\varphi_\nu(\omega)$ is calculated from the phase shift between the lateral and longitudinal strains, e.g. [44,45]. In Fig. 18, it can be observed that for UHPC the loss factors (phase shift) are small and only slightly dispersive with the frequency increases. At around f = 300 Hz, a resonance effect of the setup could be observed. Such resonance effects are inherent in those experimental investigations and could not be avoided. The results of frequency-dependent complex Young's modulus are reported for UHPC in two states, undamaged and fatigue damaged. The properties of the material in the undamaged state are higher than those in the fatigue damaged state. Furthermore, the complex Young's modulus increases with increasing frequency for both states. Conversely, as the frequency increases, the Poisson's ratio tends to remain constant for all states, and

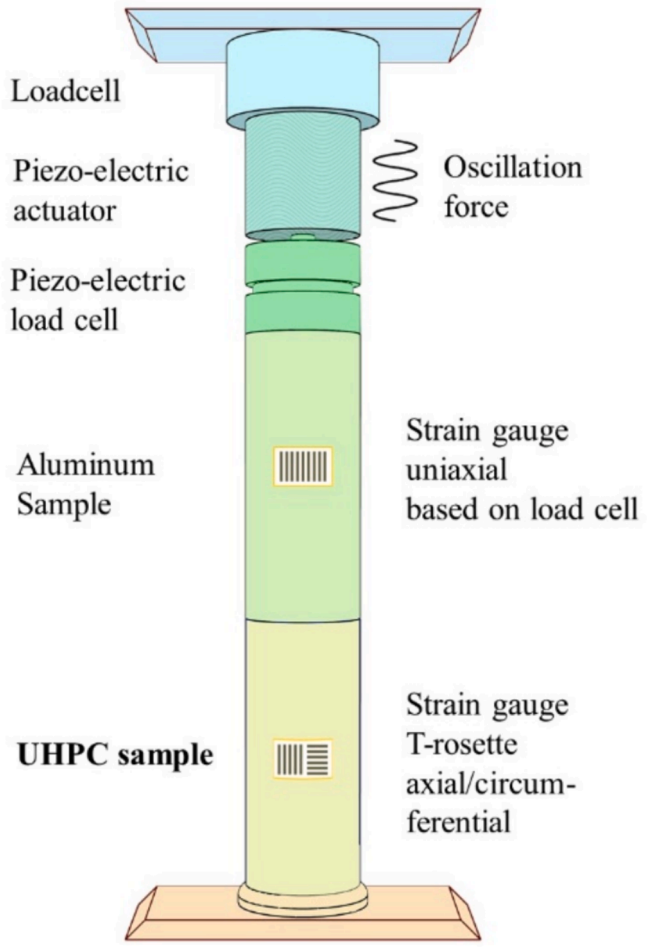

Fig. 17. Schematic sketch of the forced oscillation setup / DMA setup.

its range of variation is very small. Each sample has been tested three times. The dotted lines indicate replicated results. There is an open access version of the described and discussed measurement results shown in Fig. 18 availabe in the Data Repository of the University of Stuttgart (DaRUS) [47].

4.9. Gas sorption

Dynamic vapour sorption (DVS) is a gravimetric technique that measures the quantity, and how quickly water vapor is adsorbed and/or absorbed by a material, such as a cement paste matrix of a concrete. DVS system works by flowing precisely controlled concentrations of water vapours in dry air over a sample at a known flow rate and temperature. The sample itself rests on a digital microbalance which detects the adsorption or desorption of water vapor through the increase or decrease in mass of the material as the relative humidity varies. Compared to traditional methods, DVS provides a relatively quick way of obtaining the water vapor sorption and desorption isotherm for porous material (few days versus weeks to months). Using DVS instrument the sample can weigh between 1 mg and 4 g depending on the weighing mechanism of the ultra-sensitive recording microbalance. In principle changes in sample mass lower than 1 part in 10 million can be measured. To minimize equilibrium time, very small sample sizes (typically 10 mg) are used. The operation of the DVS takes place with a fully automated DVS control software package. This allows to analyse vapor sorption processes under dynamic conditions, where the sample is placed on an ultra-accurate mass balance in a controlled environment. The relative humidity (RH) of the sample chamber is increased gradually, for example, in 10 % RH steps from 0 % RH to 95 % RH. As the sample absorbs the solvent (water vapor), its mass increases, which is measured by the balance. After the maximum humidity has been reached, the process can be reversed to see how the mass changes with decreasing humidity. The resulting graph will yield information on the absorption and desorption characteristics of the sample as shown in Figs. 19-22.

The investigations described below were carried out with a DVS system from POROTEC. The used software package is DVS Win Version 2.18. Two samples damaged by fatigue loading (PK2_1 and PK8_1) and two undamaged samples (PK2_2 and PK8_4) were analysed. From each sample, a small quantity of material was taken from two different locations (disc 9 and 10). Therefore, in total 8 samples were investigated. All samples are from one batch, whereby the test specimens PK2 were concreted before the test specimens PK8.

The following diagrams show the changes in mass of the samples as a function of relative humidity. In Figs. 19 and 20, the fatigue damaged sample PK2_1 is compared to the undamaged sample PK2_2 with disc 9 (Fig. 19) and disc 10 (Fig. 20). In Figs. 21 and 22, the fatigue damaged sample PK8_1 is compared with the undamaged sample 8_4.

With the exception of Fig. 22, the results show a trend that the analyzed material of the fatigue damaged samples (solid, red) has a lower moisture absorption than the undamaged material (black, dashed). At 80 % RH, all analysed samples showed a significant increase. This increase is due to the effect of capillary condensation. It is known that the confinement in porous media introduces significant effects to many physical properties of fluids entrapped inside the pores including the phase equilibria [48]. Due to the strong interaction between a solid wall of pores and vapor in the confined space, phase transitions such as capillary condensation occur at temperatures and pressures different from those outside the pores [49]. For example, the vapor pressure of water vapor generally decreases in the confining pores. This means, the vapor phase of the fluid condenses at a lower pressure at a fixed temperature than it does in the bulk phase outside the porous medium. According to the Kelvin equation, capillary condensation in the cementitious materials can start at a relative humidity of more then 50 % RH in pores. For an estimation of the order of magnitude of the confinement at which capillary condensation occurs, in [50] it is considered, that in case of water vapor at room temperature with a surface tension of $\gamma_{lv} = 72\text{mJ/m}^2$ and, $\rho\text{l} = 5.5 \times 10^4\ \text{mol/m}^3$, and an assumed contact angle of $\theta = 30^\circ$ in ambient conditions with a relative humidity of $P_v/P_{sat} = 40$ % RH, one has a Kelvin radius associated to the undersaturation of $r_k \simeq 0.6$ nm and a distance of the parallel solid surfaces of the nanopores with $D_c \simeq 1$ nm. It is obvious that the scale is in the range of the Kelvin equation, and increases quickly with humidity. So, it reaches 4 nm at 80 % RH and 18 nm at 95 % RH. Therefore, capillary condensates are ubiquitous in ambient conditions. Only adsorption takes place below this value. [51,52].

Therefore, a lower amount of adsorbed moisture at higher relative humidities observed at the damaged samples due to fatigue loading as shown in Figs. 19-21 illustrates that the volume of nanopores has decreased compared to the specimens which were not subjected to fatigue loading. It is known from [53] that fatigue stresses lead to larger pores in the cement stone which equally indicates a reduction of the inner surface area.

It is assumed that the nanopores in the cement gel, which occur mainly in the C-S-H phases, coalesce into larger “collective pores” as a result of the fatigue loading. The C-S-H phases must be therefore realigned at a closer distance from each other. The result should be a denser material structure around these collecting pores.

This effect can also be explained in more detail by interpreting the TEM-results in Chapter 4.2. Fatigue damage causes the morphology to become denser and dark material contrasts to form in the cement paste matrix, which indicates a very low density in that area. The adjacent material is compacted in the process and seems to be brighter. This results in a decreasing volume of nanopores as shown with the sorption

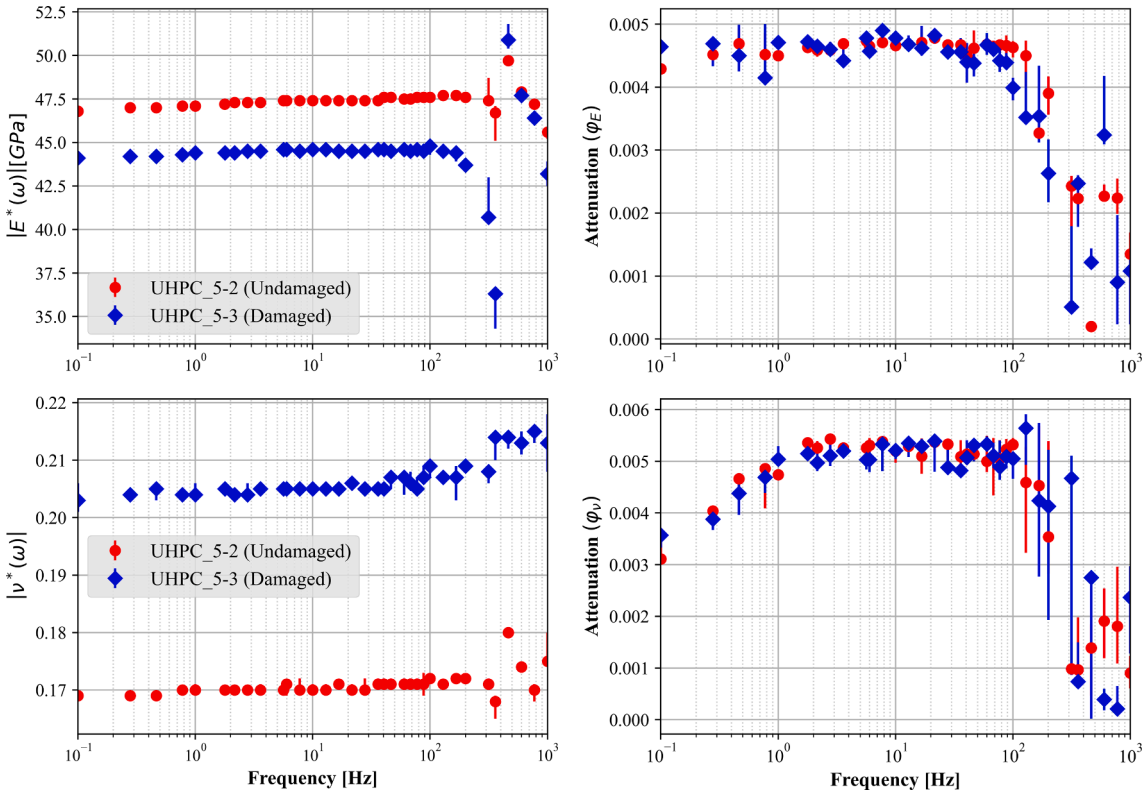

Fig. 18. Left: Results of the absolute value of the frequency-dependent Young's modulus and the absolute value of the frequency-dependent Poisson's ratio. Intrinsic attenuation (loss factor) $\varphi_E \approx \tan\varphi_E = E''/E'$ and $\varphi_\upsilon \approx \tan\varphi_\upsilon = \upsilon''/\upsilon'$.

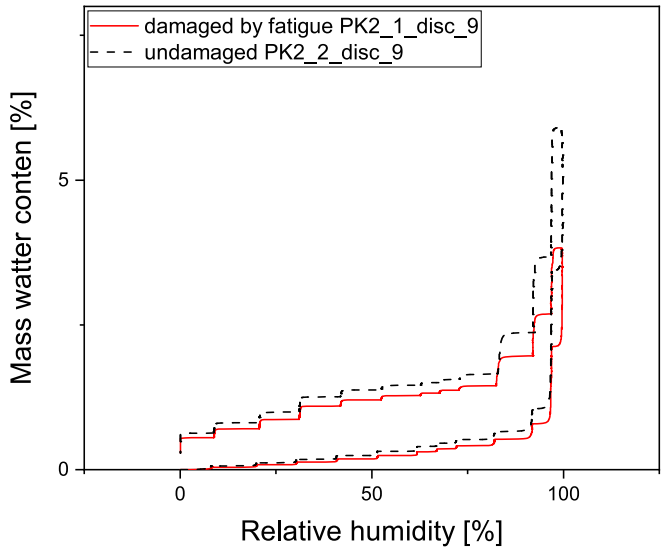

Fig. 19. Changes in mass as a function of relative humidity for the fatigue damaged sample PK2_1 and undamaged sample PK2_2 (disc 9).

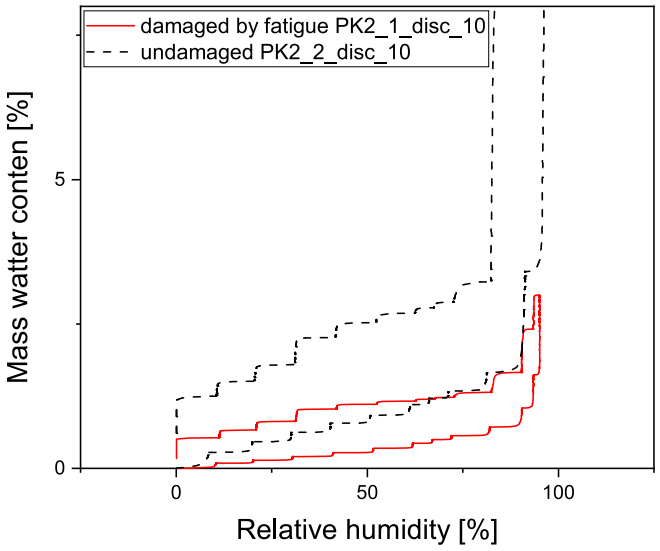

Fig. 20. Changes in mass as a function of relative humidity for the fatigue damaged sample PK2_1 and undamaged sample PK2_2 (disc 10).

isotherms in Figs. 19-21. The DVS can therefore be used to detect fatigue-related changes in the cement paste on a nanopore size scale of up to 18 nm.

Due to the small number of sample results, additional data should be collected to confirm the assumptions made.

4.10. Measurements of porosity and pore structure

The UHPC before and after fatigue loading was investigated by mercury intrusion porosimetry (MIP), by measuring the free water uptake (DIN EN 14617–1 [54]), and the water uptake under vacuum (DIN EN 772–4 [55]). The samples for the water uptake were dried at 70 °C before. Disc-shaped samples of 1 cm thickness were used. It was necessary to dry the specimens for 99 days, because of their high

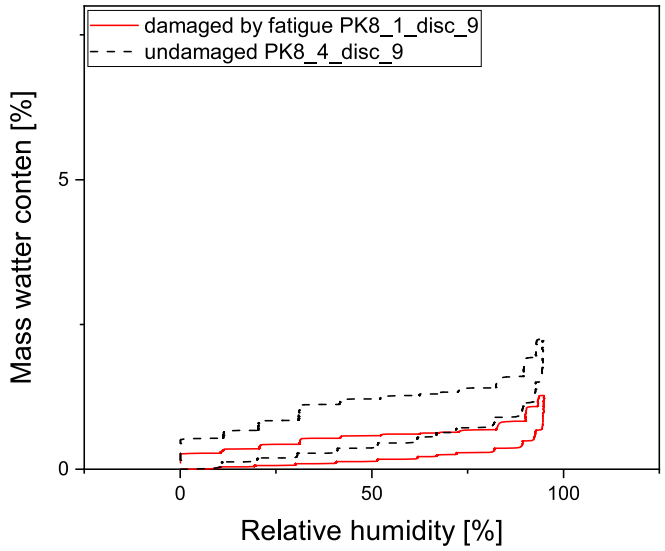

Fig. 21. Changes in mass as a function of relative humidity for the fatigue damaged sample PK8_1 and undamaged sample PK8_4 (disc 9).

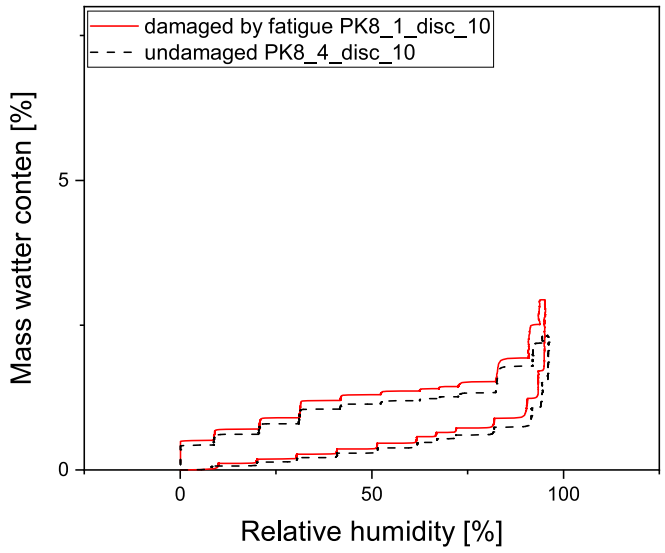

Fig. 22. Changes in mass as a function of relative humidity for the fatigue damaged sample PK8_1 and undamaged sample PK8_4 (disc 10).

impermeability. The undamaged specimens showed a weight loss of 5.36 ± 0.13 % (4 specimens), the fatigue damaged specimens a weight loss of 5.27 ± 0.12 % after 99 days (5 specimens). No significant difference between specimens before and after fatigue loading was observed. The free water uptake and the water uptake under vacuum experiments showed a water uptake with decreasing rate until about 57 days for all samples. At this time the free water uptake amounts to 2.55 ± 0.22 w.-% before fatigue loading and 2.53 ± 0.08 w.-% after fatigue loading, and the water uptake under vacuum amounts to 2.69 ± 0.24 w.-% before fatigue loading and 2.72 ± 0.23 w.-% after fatigue loading. As to be expected there is a small difference between the free water uptake and the water uptake under vacuum, but no significant difference between specimens before and after fatigue loading. After that a slow further increase in weight is observed without significant differences between the samples with and without fatigue. The weight loss by drying was not reached after 500 days of water uptake. Fig. 23 shows typical curves.

The principle of MIP is to increase the mercury pressure around the specimen and to measure the intruded volume as a function of pressure. The higher the pressure the smaler the pores filled. With the washburne equation the mercury pressure is converted into a pore radius. In spite of the known disadvantages of the method (unknown contact angle, assumed here to 140° (DIN ISO 15901 [56]) and assumptions on the pore shape, ink-bottle effect) the method is a powerful tool to get information about the pore structure. For further information on the method see [31].

For the MIP measurements a „Pascal 440“ by „Thermo Fisher Scientific instrument“ was used. The specimens were dryed at 40 °C in vacuum. Measurements were performed using a step mode. Table 7 shows the results. Fig. 24 shows the cumulative pore volume of the UHPC. A significant difference between the samples before and after fatigue loading was not observed. Another investigation in a second laboratory gave the same result. In addition it should be mentioned that in the case of a normal strength concrete Tomann [57] observed an increase of the total pore surface due to fatigue loading until failure, especially in case of a high water content in the specimen. It should be mentioned, that in addition the UHPC contains a coarse porosity, that can not be measured by MIP.

4.11. Micro-/nanoindentation

A key question to be solved in this research was, how a fatigue loading will influence the mechanical properties of concrete and especially of its constituent hardened cement paste on a microstructural level. Here, it is especially interesting to study, at which scale level fatigue damage can actually be observed. Herefore, nano- as well as microindentation testing was carried out. Both techniques consist of probing the samples surface with a diamond indenter tip, by applying a force perpendicular to the samples surface, thus indenting the mineral phases present at the indentation spot. With regard to the question, which scale levels are influenced by fatigue, it must be noted that nanoindentation probes a volume of approx. 1 μm^3 whereas in microindentation, a much larger volume of up to 0.1 to 0.2 mm^3 is probed.

From the load-deformation (i.e. the load-indentation) curve (see Fig. 25a), information on the stiffness (indentation modulus M) and hardness H can be determined [58]. As hardened cement paste and concrete are highly heterogeneous at the mentioned scale levels, statistical indentation was carried out, yielding information on the mechanical heterogeneity of the samples on a microstructural level (see e.g. [59]). Similar experiments have e.g. been carried out to study the effect of low w/c ratio [60], the partial substitution of cement by calcined clays [61] and the processes occurring during concrete creep [62,63].

The microstructure of hardened cement paste is primarily responsible for the mechanical properties of the concrete. It develops during hydration resulting mainly in the formation of Calcium-Silicate-Hydrates (C-S-H) and Calcium Hydroxides (CH). The effect of a fatigue loading onto the mechanical properties of these phases currently is unknown and was therefore of key interest in this study. By coupling nanoindentation results with mechanical models, such as presented in [62], information on a scale level as low as < 10 nm can be drawn (see e. g. [63]).

In this study, cylindrical specimen slices with a height of 10 mm and a diameter of 60 mm were extracted from the large concrete samples and again cut into 4 segments. After cutting, each slice was stored in a climate chamber under a nitrogen atmosphere with a relative humidity of 33 % to prevent carbonation effects. Directly before testing, the surfaces of the samples were grinded and polished using SiC papers in order to achieve an even surface to get repeatable results [64].

The microindentation measurements were carried out using a micro combi tester machine (Anton Paar MCT^3) with a 4-sided Vickers tip. For each sample, a total of 225 indentations were conducted within a 15 x 15 grid (spacing 400 μm) dispersed across the sample surface. The indentations were applied force-controlled using a trapezoidal load history with a maximum deformation of 25 μm and a 10-second holding

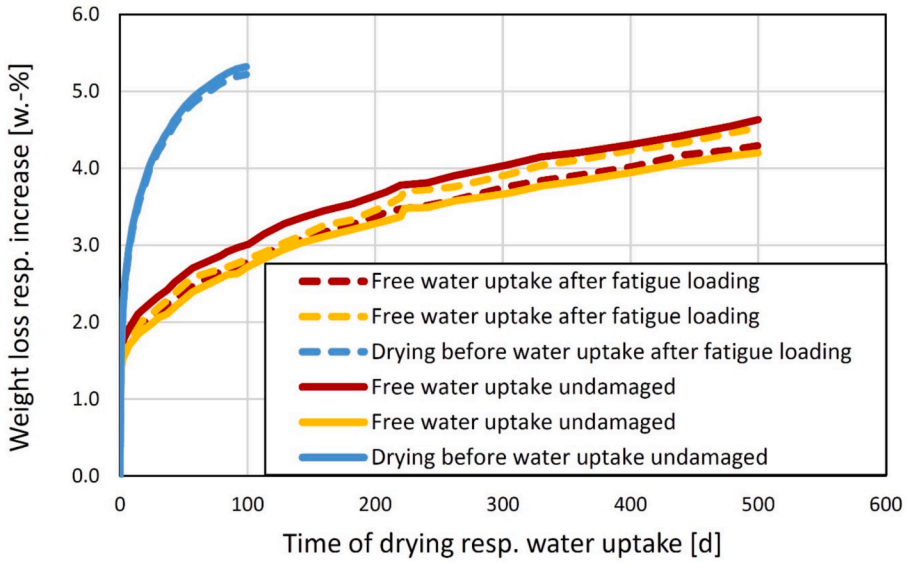

Fig. 23. Drying and free water uptake of samples. The kink at 223 days in curves PK2_1-b and PK2_2-b is caused by a water-storage at 150 bar for two days.

Table 7
UHPC, results of MIP.

	Undamaged sample	Fatigue damaged sample
Number of specimens	4	4
Total pore volume [mm^3/g]	12.5 ± 2.0	12.2 ± 3.0
Total pore surface [m^2/g]	2.8 ± 0.7	2.3 ± 0.4
Average pore diameter [nm]	18.5 ± 2.5	22.0 ± 7.4
Medium pore diameter [nm]	426 ± 411	679 ± 598
Modal pore diameter [nm]	5.18 ± 0.52	4.90 ± 0.01
Porosity [vol.-%]	2.86 ± 0.44	2.75 ± 0.64
Bulk density [g/cm^3]	2.28 ± 0.04	2.27 ± 0.06
Bulk density (measured by weighting under water) [g/cm^3]	2.23 ± 0.1 (n = 5)	2.34 ± 0.1 (n = 4)

phase at maximum load. The loading and unloading rate were kept constant at 10 N/min. The nanoindentation measurements were conducted using a Anton Paar NHT^3 nanoindentation tester machine with a 3-sided Berkovich tip. A total of 625 indentations was applied to each sample within a 25 x 25 grid, spaced at 15 µm. The tests were performed force-controlled at a maximum load of $F_{max} = 5$ mN and at a loading and unloading rate of 0.03 N/min, see Fig. 25(a).

Two material properties are analysed in this study as indicators of fatigue damage: the indentation hardness *H*, which correlates with the strength of the material, and the indentation modulus *M*, which is related to the modulus of elasticity of the material (details on data evaluation etc. see [63]). The mechanical properties determined by nanoindentation are analysed using a Gaussian Mixture Model approach coupled to a micromechanical model [62]. The results reveal the presence of five clusters representing five different phases in the investigated concrete. For further analysis and discussion, the paper will focus on the two types of C-S-H phases (low density (LD) with low packing density and high density (HD) with high packing density; [65]), as these are mainly responsible for the mechanical properties. Fig. 25 (b) and (c) illustrate the distribution of the indentation modulus *M* determined by nanoindentation on one representative fatigued specimen.

No significant impact of fatigue damage on the results determined by microindentation could be observed (not shown). In contrast, with nanoindentation some differences were observable. The influence of the fatigue damage on the mechanical properties of LD- and HD-C-S-H phases are illustrated in Fig. 26. It can be seen that the mean value of indentation hardness as well as of the indentation modulus of all three samples are decreased slightly due to fatigue loading. Interestingly, a strong decrease of the mechanical properties of high-density C-S-H phases due fatigue loading is visible. However, the influence of fatigue damage on both mechanical properties of HD-C-S-H phases are still in scattering range.

Overall, the results indicate that fatigue loading leads to a deterioration of the micromechanical properties of cement paste. This influence is particularly visible in the results obtained with nanoindentation measurements, suggesting that fatigue damage occurs within a scale range significantly below one micrometer. Moreover, there are indications that fatigue damage takes place in the densest structures (HD-C-S-H), leading to a decrease in stiffness and hardness. As LD-C-S-H phases have a representative size below approx. 20 nm and HD-C-S-H is understood to be even smaller in size (see [65]), there is substantial indication that it is this scale level which is affected by fatigue. In summary, indentation (especially nanoindentation) seems to be a suitable method for characterizing fatigue damage in the microstructure of concrete and identifying the mechanisms responsible for the damage. However, there are several challenges especially concerning the considerable scatter of the results. Here, extended research by the authors on pure hardened cement paste shows a significantly reduced noise, confirming the above results.

4.12. Acoustic emission techniques

Following [66] acoustic emission techniques (AET) are different from other non-destructive testing methods (NDT) because it is usually applied during loading. A structure or structural part can be tested under real load conditions (or similar to these) and AET is able to detect a failure due to fatigue inside this structure at a very early stage, long before it completely fails. AET detects the elastic waves radiated by a growing fracture. It usually identifies defects while they develop during the test – the defect quasi "produces" the test signal. These characteristic features of the AE method result in advantages as well as disadvantages.

An advantage of AE techniques is that damage processes in materials being tested can be observed during the entire load history, without any disturbance to the specimen. AE studies require that under favorable conditions only a few sensors are able to monitor the AE activity of a structure, provided there are sufficiently strong signals to cross a threshold called trigger level. The sensors can be fixed to the surface of the specimen for the duration of the test and do not have to be moved to scan the whole structure point by point. Access to both sides of an object,

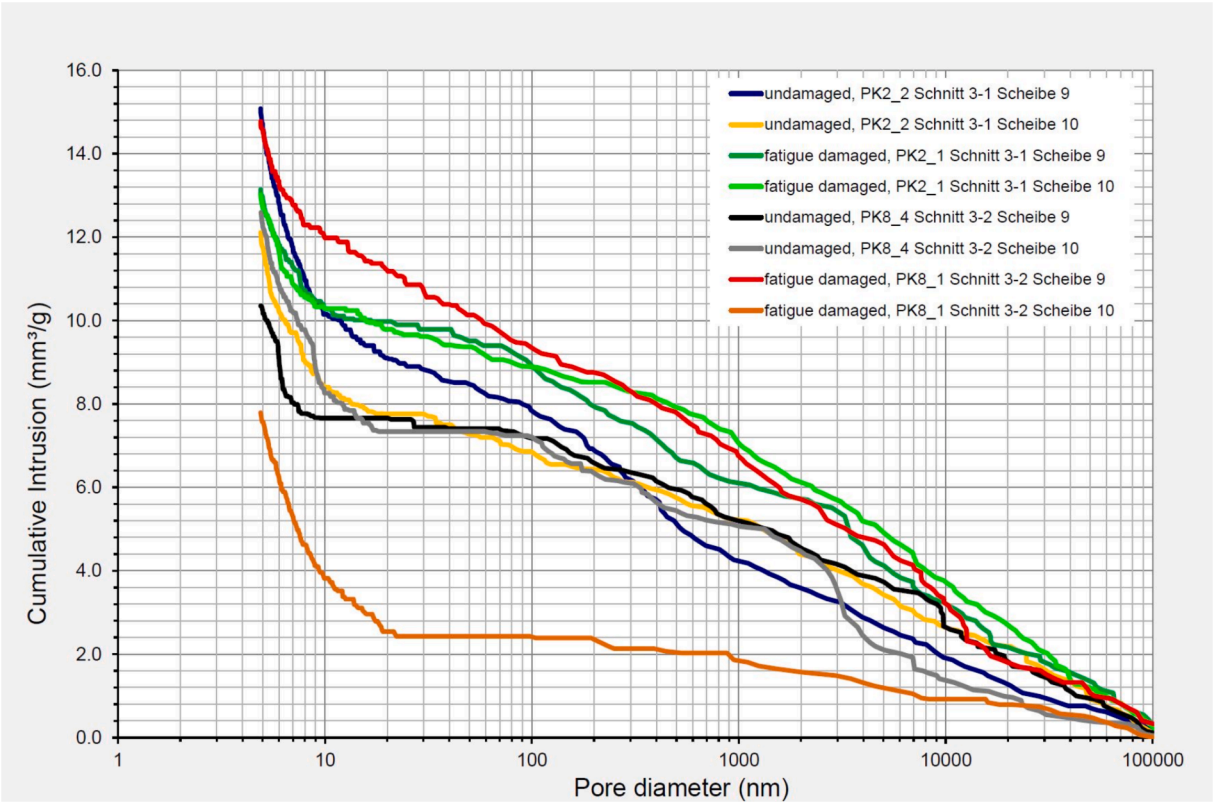

Fig. 24. UHPC, mercury intrusion porosimetry.

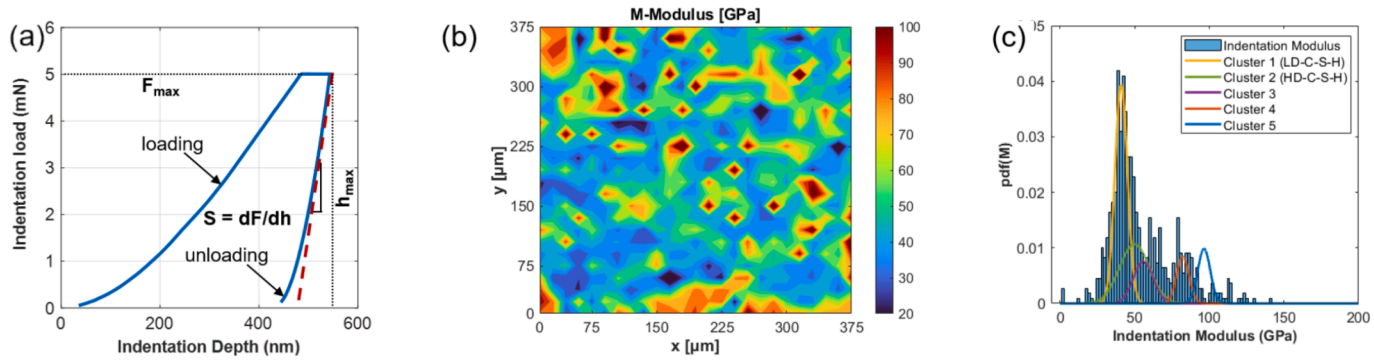

Fig. 25. (a) Characteristic load-deformation curve representative of the nanoindentation. (b) Characteristic distribution of the indentation modulus of an exemplarily specimen. (c) Probability density and deconvolution of indentation modulus M in five phases (LD-C–S–H, HD-C–S–H, a mix phase of LD-C-S-H intertwined with CH and quartz and clinker).

which is necessary for all through-transmission methods, is not required in AET.

A disadvantage of the AET method is that a particular signal is not perfectly reproducible due to the nature of the signal source, e.g. the sudden and sometimes random formation of a crack. Although specimens of the same shape and same material properties should cause similar AE activities under load, this is not always the case. Materials with scattered inhomogeneities (like fibers in concrete) of a particular dimension, will not give similar AE results if the wavelength of the signals is of a similar size as the heterogeneities. This is one of the reasons why it is useful to compare the results of acoustic emission tests with other testing methods, for example using a visual inspection of the surface (digital image correlation techniques), ultrasound methods, X-Ray, or RADAR.

Another point addresses the energy released by acoustic emissions. Signals – in particular those used as precursors of failure – are usually several magnitudes smaller compared to signals used in ultrasonic techniques. This requires much more sensitive sensors as well as reliable amplifiers and pre-amplifiers. Problems related to this are the influence of ambient noise, the attenuation of signals, and the probably resulting low signal-to-noise ratio. It requires sophisticated data processing techniques to detect acoustic emissions, to localize them, and to apply other advanced techniques or inversions. A reliable analysis of acoustic emission signals and the interpretation of the data in material testing are very often only possible in cases where the signals have been localized successfully. Signal localization is the basis of most analysis techniques used in AE based on signal recordings. The sources of acoustic emissions can have widely varying characteristics due to significant differences in the source signals. These differences get more pronounced using non-resonant transducers and after separating signals from noise, which can arise from artificial or natural sources with origins inside or outside the tested object.

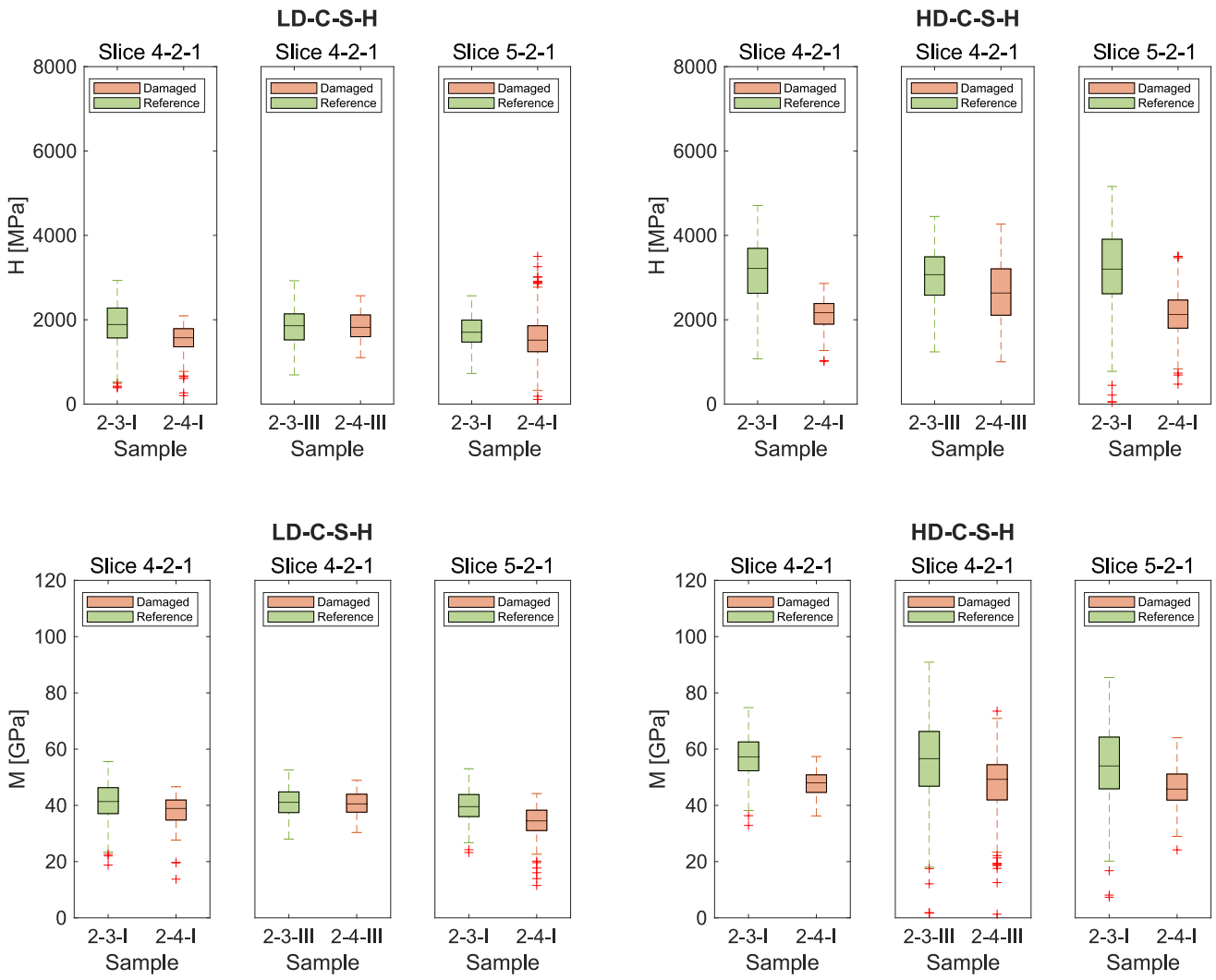

Fig. 26. Indentation hardness H and modulus M of LD and HD-C-S-H phases of reference samples (not damaged) and damaged samples extracted from larger concrete slices determined by statistical nanoindentation.

AET can be divided into two main groups: parameter-based (classical) and signal-based (quantitative) AE techniques [67]. If AE events are recorded with one or more sensors, such that a set of parameters are extracted from the signal and later stored but the signal itself is not stored, the procedure is usually referred to as a parameter-based (or classical) AE technique. Some typical AE parameters extracted by conventional AE equipment are the maximum peak-to-peak amplitude, the arrival time (defined as the first crossing of a given amplitude threshold), the rise time (defined as the duration between the arrival time and the time where the maximum amplitude is recorded) and the

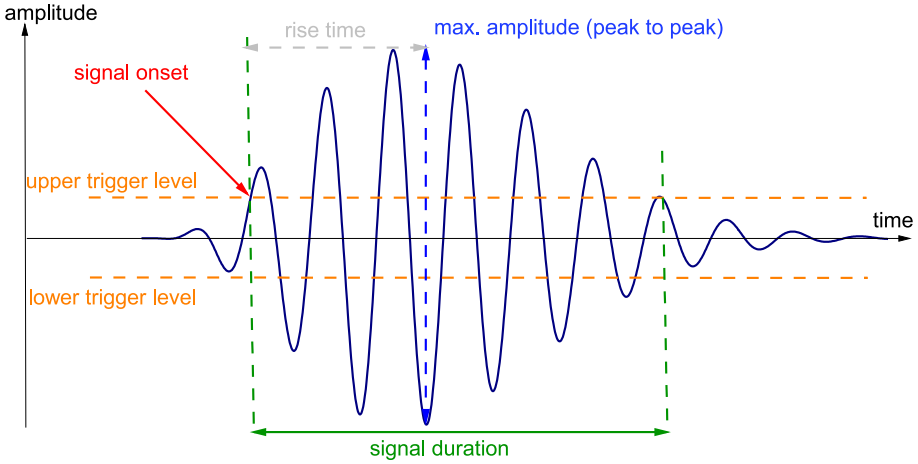

Fig. 27. Definition of parameters of an AE signal [66].

duration (defined by the last crossing of a given amplitude threshold) [68]. A typical signal measured (but not stored) in AE analysis using the classical approach is given in Fig. 27.

If a signal-based approach is used, the waveforms recorded by the sensors (preferably sensors with a broadband frequency response) need to be analyzed. A suite of analysis procedures exists to evaluate fracture parameters [66]. The first step in the analysis is usually the 3D localization of the sources of AE signals. More advanced analyses may then be applied, for instance, source mechanism calculations. For localization techniques see [69]. More sophisticated AE techniques are related to waveform inversions or inversions onto the moment tensor. This could give insight into the fracture size, orientation, and fracture mode (so-called Mode I, II, or III). A comprehensive representation of the state of the art in AET can be found in Grosse et al. [66] and the included references of the individual chapters. Applications of AET in regard to short and long-fiber reinforced concrete can be found in the literature [70,71] as well as reports about practical applications in the field [72].

The acoustic emissions are also indicator for the evaluation of damage activity of concretes within fatigue tests. Here, one parameter is the number of AE-hits which depends e.g. on the concrete composition and the maximum stress level of fatigue loading. The cumulated numbers of AE-hits are generally lower for concretes and mortars at higher stress levels and, thus, lower numbers of cycles to failure compared to lower stress levels. However, the gradient of cumulated AE-hits, meaning the increase in AE-hits per load cycle, is steeper for higher stress levels [73].

In [72] stepwise developments of cumulated AE-hits have been found for high-strength concretes and mortars of different compositions tested at a maximum stress level of $S_{max} = 0.70$. However, these stepwise developments could not be observed at a higher stress level of $S_{max} = 0.85$ [73]. Those stepwise developments were not straight visible in the macroscopic indicators strain and stiffness development. Therefore, it was hypothesized that parts of the damage process are occurring on such very small scales (maybe sub-microscale) in the sections with a strong AE-hits increase that they are not (yet) visible in the macroscopic strain development. Furthermore, within the rather horizontal parts, equilibrium states of these parts of the damage process might be reached within the microstructure [73].

In Fig. 28, single curves of the cumulated AE-hits are shown with respect to the relative numbers of cycles to failure N/N_f for the three UHPC-specimens tested at a maximum stress level of $S_{max} = 0.75$ until fatigue failure. It is visible that the developments of cumulated AE-hits also contain steps within their slopes similar to the findings in [73]. Furthermore, the number of AE-hits increases significantly at the end of the fatigue tests.

However, meanwhile it became clear that the simple counting of AE-hits has only a very limited significance with regard to the damage processes in the microstructure of concrete. In addition, the characteristics of the AE-hits have to be considered in the analyses to gain insights into damage processes. The clustering technique using Gaussian mixture modelling is a promising analysing method which was firstly applied to the AE-hits caused by compressive fatigue loading in plain concrete [13]. Hereby, the AE-hits were assigned to two different clusters which are possibly related to two different damage mechanisms based on the parameters AF (average frequency) and RA (rise time/amplitude). In experiments with high-performance concrete the clusters can be related to the phases of fatigue, so that the change from phase II to phase III can be determined with AET. In addition, AET also shows in this case, that in dry specimens hits are generated mainly at maximum stress level, in moist specimens mainly at minimum stress level. This permits an insight in details of the damage process.

5. Conclusions and useful (combinations of) methods to examine the fatigue damage in concrete

The compressive fatigue of ultra-high strength concrete results first

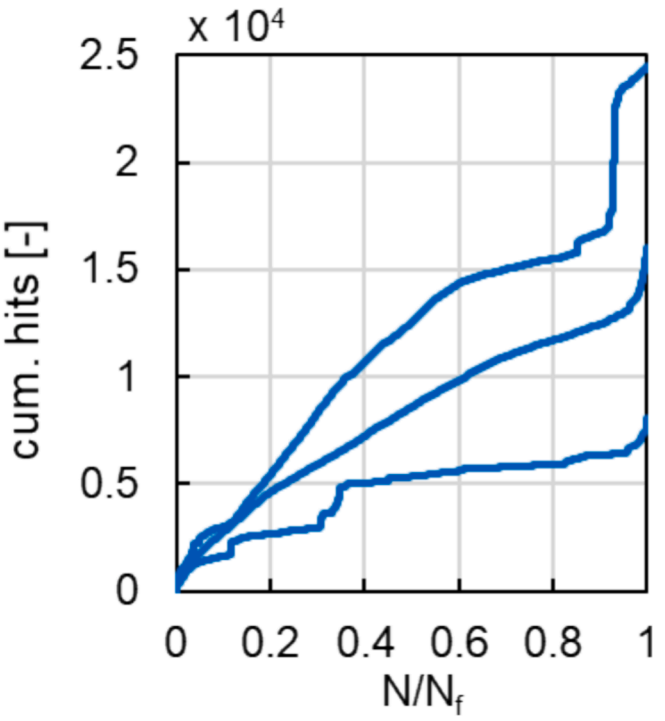

Fig. 28. Developments of cumulated AE-hits of the UHPC at $S_{max} = 0.75$. N/Nf: relative numbers of cycles to failure.

in alterations of the binder on the nano-scale, distributed across the concrete (densification of the C-S-H, alteration of ettringite). Some of these alterations change into damages on the nanoscale (nanocracks) with further fatigue loading. These alterations and damages can only be observed directly with Transmission Electron Microscopy (TEM). TEM examinations of concrete require the Focus Ion Beam (FIB) technique to prepare suitable specimens (TEM lamellae). An additional significant advantage of TEM is the possibility of chemical element analysis with a spatial resolution in the nanometer range.

These alterations and damages on the nanoscale also result in a coarsening of the pore structure that are indirectly observable in the results of gas sorption techniques, for example Dynamic Vapour Sorption (DVS). In addition some changes in the C-S-H-structure seem to be observable with special techniques of Infrared Spectroscopy (IR), but not with Raman Spectroscopy up to now. With Thermogravimetric Analysis (TGA) a significant change of water content due to the fatigue loading is measurable as well. This can be a side-effect of a temperature-increase and further hydration during the fatigue loading. Although, with TEM, changes of ettringite were identified as one of the alterations on the nanoscale, no significant changes of the X-ray powder diffraction signals due to the fatigue experiments on UHPC could be observed.

In macroscopic experiments, fatigue loading results in measurable changes of the mechanical properties. With Dynamic Mechanical Analysis (DMA) experiments on a smaller scale, the complex Young's modulus and the complex Poisson's ratio can be computed. With microindentation no significant changes by fatigue loading could be observed. But with nanoindentation the fatigue damage result in reduced indentation hardness and indentation modulus of the HD-C-S-H-phase while the LD-C-S-H-phase seems unaffected.

Within the priority programme SPP 2020 "Cyclic Deterioration of High-Performance Concrete in an Experimental-Virtual-Lab" the Acoustic Emission Technique (AET) was helpful to get information on the damage process during ongoing fatigue loading. The clustering of signals by their characteristics shows different type of signals in the different phases of fatigue. AET also shows a very different damage behaviour of dry and moist materials. Often AET appears to be more

sensitive to the fatigue progress than macroscopic damage indicators.

With preceeding fatigue loading, damages on the nanoscale will transform to cracks, first on the microscale and later, on the macroscale. The higher the strength of the concrete, the later such cracks will occur. In the case of the UHPC examined here, no significant difference between specimens with (beginning of phase III) and without fatigue loading could be observed with X-ray computed tomography (XCT). Of course, the different components of concrete, including fibres and pores are observable with XCT. However, the XCT-technique does not perform as well as expected with respect to damage in the concrete microstructure at the beginning of the priority programme SPP 2020.

Microcracks are also visible with light microscopy. The number of cracks in the UHPC specimens after fatigue loading appears to be higher than before. This is proven for HPC. In addition, polarized light microscopy is an excellent technique for phase and microstructure analyses on the micrometer scale. A vacuum treatment of the specimens is not necessary. Therefore, no shrinkage cracks occur in contrast to classical scanning electron microscopy (SEM). In TEM examinations, shrinkage cracks are not a problem because a TEM lamella is very small and will usually be extracted between shrinkage cracks.

Investigations of the drying behaviour, the free water uptake, the water uptake under vacuum and by mercury intrusion porosimetry (MIP) showed no significant difference between the UHPC before and after fatigue loading. However, this will be the case with lower-strength materials and with specimens very close to breakage.

CRediT authorship contribution statement

Michael Engelhardt: Writing – original draft, Investigation, Conceptualization. **Andreas Kalytta-Mewes:** Writing – original draft, Investigation, Conceptualization. **Dirk Volkmer:** Writing – review & editing, Writing – original draft, Project administration, Methodology, Funding acquisition, Conceptualization. **Jessica Lohmann:** Writing – original draft, Investigation, Conceptualization. **Martin Ritter:** Writing – review & editing, Project administration, Methodology, Funding acquisition, Conceptualization. **Gunnar Schaan:** Writing – review & editing, Writing – original draft, Methodology, Investigation, Conceptualization. **Frank Schmidt-Döhl:** Writing – review & editing, Writing – original draft, Project administration, Methodology, Investigation, Funding acquisition, Conceptualization. **Mohamed Abubakar Ali:** Writing – original draft, Investigation, Conceptualization. **Marco Basaldella:** Writing – original draft, Investigation, Conceptualization. **Michael Haist:** Writing – review & editing, Writing – original draft, Project administration, Funding acquisition, Conceptualization. **Bianca Kern:** Writing – original draft, Project administration, Investigation, Conceptualization. **Ludger Lohaus:** Writing – review & editing, Project administration, Methodology, Funding acquisition, Conceptualization. **Nadja Oneschkow:** Writing – review & editing, Writing – original draft, Project administration, Methodology, Funding acquisition, Conceptualization. **Corinna Rozanski:** Writing – original draft, Investigation, Conceptualization. **Tim Timmermann:** Writing – original draft, Investigation, Conceptualization. **Christian U. Grosse:** Writing – original draft, Project administration, Methodology, Funding acquisition, Conceptualization. **Veit Birtel:** Writing – original draft, Investigation, Conceptualization. **Harald Garrecht:** Writing – review & editing, Writing – original draft, Project administration, Methodology, Funding acquisition, Conceptualization. **Hamid Madadi:** Writing – original draft, Investigation, Conceptualization. **Martin Markert:** Writing – original draft, Investigation, Conceptualization. **Holger Steeb:** Writing – review & editing, Writing – original draft, Project administration, Methodology, Funding acquisition, Conceptualization.

Declaration of competing interest

The authors declare that they have no known competing financial interests or personal relationships that could have appeared to influence the work reported in this paper.

Acknowledgments

This research was funded by the Deutsche Forschungsgemeinschaft (DFG), as part of the priority program “SPP2020: Cyclic damage processes in high-performance concretes in the Experimental Virtual Lab” (313829475) and using major research instrumentation (457308988; 457309087, 259770612, 259780909) funded by DFG.

Statements and declarations.

Fatigue tests and material preparation was mainly done by M. Basaldella, M. Jentsch, B. Kern.

Ethics approval.

Not applicable.

Editorial Board Members and Editors competing interests.

Not applicable.

Employment competing interests.

Not applicable.

Financial or non-financial interests.

The authors have no relevant financial or non-financial interests to disclose.

Appendix A. Supplementary data

Supplementary data to this article can be found online at https://doi.org/10.1016/j.ijfatigue.2025.109038.

Data availability

Data will be made available on request.

References

[1] European Committee for Standardization (2023) FprEN 1992-1-1: 2023 (E): Eurocode 2 - Design of concrete structures - Part 1-1: General rules and rules for buildings, bridges and civil engineering structures. Brussels.
[2] Fédération International du Béton (ed.) (2023) fib model code for concrete structures 2020, Lausanne. ISBN: 978-2-88394-176-2.
[3] Lohaus L, Oneschkow N. Cyclic deterioration of high-performance concrete – Findings of the priority programme SPP 2020. 21. Int. Baustofftagung (ibausil). Weimar, ce/papers 2023;6:833–43. https://doi.org/10.1002/cepa.2834.
[4] Basaldella M, Jentsch M, Oneschkow N, Markert M, Lohaus L. Compressive fatigue investigation on high-strength and ultra-high-strength concrete within the SPP 2020. Materials 2022. https://doi.org/10.3390/ma15113793.
[5] Basaldella M, Oneschkow N, Lohaus L. Influence of the specimen production and preparation on the compressive strength and the fatigue resistance of HPC and UHPC. Mater Struct 2021. https://doi.org/10.1617/s11527-021-01696-9.
[6] Schmidt M, Fehling E, Fröhlich S, Thiemicke J (2014) Sustainable building with ultra-high performance concrete – Results of the german priority programme 1182 funded by Deutsche Forschungsgemeinschaft (DFG). Structural Materials and Engineering Series 22 Kassel University Press, Kassel.
[7] Delly J. Essentials of polarized light microscopy. 2nd ed. Westmont: McCrone Group; 2019.
[8] Schmidt S. Transmitted light microscopy of rock-forming minerals. Basel: Springer International Publishing; 2023.
[9] St. John DA, Poole AW, Sims I (1998) Concrete petrography. Arnold, London.
[10] Schäfer N, Gudžulić V, Breitenbücher R, Meschke G. Experimental and numerical investigations on high performance SFRC: Cyclic tensile loading and fatigue. Materials 2021. https://doi.org/10.3390/ma14247593.
[11] Schäfer N, Breitenbücher R. Microcracking of high-performance concrete under cyclic loading and the influence of the aggregate. Proc 13th fib PhD Symp Paris 275-282. 2021.
[12] Oneschkow N, Scheiden T, Hüpgen M, Rozanski C, Haist M. Fatigue-induced damage in high-strength concrete microstructure. Materials 2021. https://doi.org/10.3390/ma14195650.
[13] Lanwer JP, Empelmann M. Performance-based fibre design for ultra-high performance concrete (UHPC). Appl Sci 2022;12:8559–71. https://doi.org/10.3390/app12178559.
[14] Toumi A, Bascoul A. Mode I crack propagation in concrete under fatigue: microscopic observations and modelling. Int J Numer Anal Methods Geomech 2002;26:1299–312. https://doi.org/10.1002/nag.245.
[15] Wenzel O, Schwotzer M, Müller E, Chakravadhanula VSK, Scherer T, Gerdes A. Investigating the pore structure of the calcium silicate hydrate phase. Mater Charact 2017;133:133–7. https://doi.org/10.1016/j.matchar.2017.09.035.

[16] Barnes BD, Diamond S, Dolch WL. The contact zone between portland cement paste and glass "aggregate" surfaces. Cem Concr Res 1978;8:233–44. https://doi.org/10.1016/0008-8846(78)90012-1.
[17] Diamond S. The microstructure of cement paste and concrete – a visual primer. Cem Concr Compos 2004;26:919–33. https://doi.org/10.1016/j.cemconcomp.2004.02.028.
[18] Richardson IG, Groves GW. Microstructures and microanalysis of hardened cement paste involving ground granulated blast-furnace slag. J Mater Sci 1992;27:6204–12. https://doi.org/10.1007/BF01133772.
[19] Fonseca PC, Jennings HM. The effect of drying on early-age morphology of C–S–H as observed in environmental SEM. Cem Concr Res 2010;40:1673–80. https://doi.org/10.1016/j.cemconres.2010.08.007.
[20] Bisschop J, van Mier JGM. Environmental scanning electron microscopy as tool to study shrinkage microcracks in cement-based materials. MRS Online Proc Library 1999;589:141–6. https://doi.org/10.1557/PROC-589-141.
[21] Stuart BH. Infrared spectroscopy, fundamentals and applications, analytical techniques in the sciences. Hoboken: John Wiley & Sons; 2004.
[22] Milosevic M. Internal reflection and ATR-spectroscopy. Hoboken: Wiley; 2012.
[23] Schmidt-Döhl F, Schulenberg D, Tralow F, Neubauer J, Wolf JJ, Ectors D. Quantitative analysis of the strength generating C-S-H-phase in concrete by IR-spectroscopy. Acta Polytechnica CTU Proc 2022;33:539–45. https://doi.org/10.14311/APP.2022.33.0539.
[24] Toporski J, Dieing T, Hollricher O. Confocal raman microscopy. 2. Ed. Basel: Springer International Publishing; 2018.
[25] Garbev K, Stemmermann P, Black L, Breen C, Yarwood J. Structural features of C-S-H (I) and its carbonation in air - A Raman Spectroscopic study. Part I: Fresh Phases. J Am Cer Soc 2007;90:900–7.
[26] Keshavarz L, Ghaani MR, Saremi O, English N. Characterization of nanoporous materials. In: Uthaman AU, Sabu T, Tianduo L, Hanna M, editors. Adv functional porous materials. 1. Ed. Cham: Springer (Engineering Materials); 2022. p. 319–51.
[27] Bragg WH, Bragg WL. The reflection of X-rays by crystals. Proc R Soc Lond *A* 1913;88(605):428–38. https://doi.org/10.1098/rspa.1913.0040.
[28] Lee M. X-ray diffraction for materials research - from fundamentals to applications. London: Taylor & Francis; 2017.
[29] Will G. Powder diffraction. The Rietveld method and the two stage method to determine and refine crystal structures from powder diffraction data. Berlin: Springer; 2008.
[30] Pecharsky VK, Zavalij PY. Fundamentals of powder diffraction and structural characterization of materials. 2. ed. New York: Springer; 2009.
[31] Skrivener K, Snellings R, Lothenbach B. A practical guide to microstructural analysis of cementitious materials. Boca Raton: CRC Press; 2016.
[32] Grangeon S, Claret F, Linard Y, Chiaberge C. X-ray diffraction: a powerful tool to probe and understand the structure of nanocrystalline calcium silicate hydrates. Acta Crystallogr Sect B: Struct Sci Cryst Eng Mater 2013;69(Pt 5):465–73. https://doi.org/10.1107/S2052519213021155.
[33] Tajuelo Rodriguez E, Garbev K, Merz D, Black L, Richardson IG. Thermal stability of C-S-H phases and applicability of Richardson and Groves' and Richardson C-(A)-S-H(I) models to synthetic C-S-H. Cem Concr Res 2017;93:45–56. https://doi.org/10.1016/j.cemconres.2016.12.005.
[34] Maddalena R, Hall C, Hamilton A. Effect of silica particle size on the formation of calcium silicate hydrate [C-S-H] using thermal analysis. Thermochim Acta 2019;672:142–9. https://doi.org/10.1016/j.tca.2018.09.003.
[35] Winnefeld F, Schöler A, Lothenbach B. Sample preparation. In: Skrivener K, Snellings R. Boca Raton: Lothenbach B A practical guide to microstructural analysis of cementitious materials. CRC Press; 2016. p. 29–31.
[36] Lothenbach B, Durdziński P, Weerdt KD. Thermogravimetric analysis. In: Skrivener K, Snellings R. Boca Raton: Lothenbach B A practical guide to microstructural analysis of cementitious materials. CRC Press; 2016. p. 177–211.
[37] Method and apparatus for high resolution analysis of the composition of a material - European Patent Office - EP 0494492 A2.
[38] Gill PS, Sauerbrunn SR, Crowe BS. High resolution thermogravimetry J Therm Anal 1992;38:255–66. https://doi.org/10.1007/BF01915490.
[39] Lothenbach B, Le Saout G, Gallucci E, et al. Influence of limestone on the hydration of Portland cements. Cem Concr Res 2008;38:848–60. https://doi.org/10.1016/j.cemconres.2008.01.002.
[40] Taylor HFW (2003) Cement chemistry, 2. ed., repr. Telford Publ, London.
[41] Buzug TM. Einführung in die Computertomographie – Mathematisch-physikalische Grundlagen der Bildrekonstruktion. Berlin: Springer; 2004.
[42] Otsu N. A threshold selection method from gray-level histograms. IEEE Trans Syst Man Cybern 1979;9:62–6. https://doi.org/10.1109/TSMC.1979.4310076.
[43] Feldkamp LA, Davis LC, Kress JW. Practical cone-beam algorithm. J Opt Soc Am A 1984;1:612–9.
[44] Madadi H, Steeb H. The high cycle fatigue testing of high-performance concretes using high frequency excitation. Proc Appl Math Mech 2023. https://doi.org/10.1002/pamm.202200221.
[45] Subramaniyan S, Quintal B, Tisato N, Saenger EH, Madonna C. An overview of laboratory apparatuses to measure seismic attenuation in reservoir rocks. Geophys Prospect 2014;62:1211–23. https://doi.org/10.1111/1365-2478.12171.
[46] Madadi H, Steeb H. High-speed fatigue testing of high-performance concretes and parallel frequency sweep characterization. Proc Appl Math Mech 2023. https://doi.org/10.1002/pamm.202300262.
[47] Madadi H, Steeb H. Micro- and nanostructural investigations of high and ultra-high performance concrete under fatigue 2023. https://doi.org/10.18419/darus-3692.
[48] Mitropoulos AC. The Kelvin equation. J Coll Interf Sc 2008. https://doi.org/10.1016/j.jcis.2007.10.001.
[49] Tan SP, Piri M. Equation-of-state modeling of confined-fluid phase equilibria in nanopores. Fluid Phase Equilib 2015;393:48–63.
[50] Charlaix E, Ciccotti M. Capillary condensation in confined media Handbook of Nanophysics -, Vol 1. Boca Raton: CRC Press; 2010.
[51] Haul R, Gregg SJ, Sing KSW. Adsorption, surface area and porosity. 2. Ed. London: Academic Press; 1982.
[52] Saeidpour M, Wadsö L. Moisture equilibrium of cement based materials containing slag or silica fume and exposed to repeated sorption cycles. Cem Concr Res 2015. https://doi.org/10.1016/j.cemconres.2014.12.005.
[53] Thiele M. Experimentelle Untersuchung und Analyse der Schädigungsevolution in Beton unter hochzyklischen Ermüdungsbeanspruchungen. University of Technology Berlin; 2015. Dissertation.
[54] DIN EN 14617-1. Agglomerated stone - Test methods - Part 1: Determination of apparent density and water absorption; German version EN 14617-1, 2013-08. Berlin: Beuth; 2013.
[55] DIN EN 772-4. Methods of test for masonry units - Part 4: Determination of real and bulk density and of total and open porosity for natural stone masonry units; German version EN 772-4,1998-10. Berlin: Beuth; 1998.
[56] DIN ISO 15901-1. Bewertung der Porengrößenverteilung und Porosität von Feststoffen mittels Quecksilberporosimetrie und Gasadsorption - Teil 1 Quecksilberporosimetrie, 2019-03. Berlin: Beuth; 2019.
[57] Tomann C. Wasserinduzierte Ermüdungsschädigung von Beton. University Hannover; 2021. Dissertation.
[58] Oliver WC, Pharr GM. An improved technique for determining hardness and elastic modulus using load and displacement sensing indentation experiments. J Mat Res 1992;7:1564–83.
[59] Ulm FJ, Abousleiman Y. The nanogranular nature of shale. Acta Geotech 2006;1:77–88. https://doi.org/10.1007/s11440-006-0009-5.
[60] Chen JJ, Sorelli L, Vandamme M, Ulm FJ, Chanvillard GA. A coupled nanoindentation/SEM-EDS study on low water/cement ratio portland cement paste: Evidence for C–S–H/Ca(OH)$_2$ nanocomposites. J Am Ceram Soc 2010;93:1484–93.
[61] Deiters M, Rozanski C, Schack T, Haist M (2023) Influence of calcined clay on micromechanical properties and creep of hardened cement paste. ce/papers 6:431-440. Doi: 10.1002/cepa.2785.
[62] Vandamme M, Ulm FJ. Nanogranular origin of concrete creep. Proc Nat Acad Sci 2009;106:10552.
[63] Haist M, Divoux T, Krakowiak KJ, Skibsted J, Pellenq RJM, Müller HS, et al. Creep in reactive colloidal gels: A nanomechanical study of cement hydrates. Phys Rev Res 2021;3:043127.
[64] Miller M, Bobko C, Vandamme M, Ulm FJ. Surface roughness criteria for cement paste nanoindentation. Cem Concr Res 2008;38:467.
[65] Jennings HM. Colloid model of C- S- H and implications to the problem of creep and shrinkage. Mat Struct 2004;37:59–70.
[66] Grosse CU, Ohtsu M, Aggelis DG, Shiotani T (Eds.) (2022) Acoustic emission testing: Basics for research applications in engineering. Springer Nature, Basel. Doi: 10.1007/978-3-030-67936-1.
[67] Grosse CU (2010) Acoustic emission. In: Maierhofer C, Reinhardt HW, Dobmann G (eds.) Non-destructive evaluation of reinforced concrete structures vol. 2: Non-destructive testing methods. Woodhead Publ, Oxford, pp 185-214.
[68] ASTM. E610 – Standard definitions of terms relating to acoustic emission. Rev 1989;89A:579–81.
[69] Kurz JH, Schumacher T, Linzer L, Schechinger B, Grosse CU. Source localization. In: Grosse CU, editor. Acoustic emission testing - basics for research - applications in engineering. Basel: Springer Nature; 2022. p. 117–72. https://doi.com/10.1007/978-3-030-67936-1_6.
[70] Reinhardt HW, Grosse CU, Kurz JH. Short fiber reinforced concrete. In: Busse G, Kröplin B, Wittel FK, editors. Damage in composite materials - simulation and non-destructive evaluation. Norderstedt: ISD-Verlag; 2006. p. 143–55.
[71] Reinhardt HW, Grosse CU, Kurz JH. Continuous fiber reinforced concrete. In: Busse G, Kröplin B, Wittel FK, editors. Damage in composite materials - simulation and non-destructive evaluation. Norderstedt: ISD-Verlag; 2006. p. 251–62.
[72] Grosse CU, Schumacher T. Anwendungen der Schallemissionsanalyse an Betonbauwerken. Bautechnik 2013;90:721–31.
[73] Oneschkow N, Timmermann T. Influence of the composition of high-strength concrete and mortar on the compressive fatigue behaviour. Mater Struct 2022. https://doi.org/10.1617/s11527-021-01868-7.